Supramolecular Assembly of Pyrene-Tetrathiafulvalene Hybrids on Graphene: Structure-Property Relationships and Biosensing Activity

Marina Garrido, Emiliano Martínez-Periñán, Joaquín Calbo, Laura Rodríguez-Pérez, Juan Aragó, Encarnación Lorenzo,* Enrique Ortí,* Nazario Martín* and Mª Ángeles Herranz*

Supporting Information

Contents

1. Materials and experimental methods

All reagents were purchased from commercial sources and used without any additional purification. 9,10-bis(1,3-dithiol-2-ylidene)-9,10-dihydroanthracene (exTTF),[1] the pyrene-exTTF system **1**,[2] as well as precursors **3**,[3] **4**[4] and **7**[5] were synthesized using previously reported procedures. Graphite for the few-layer graphene (FLG) exfoliation was purchased from TIMCAL (TIMREX SFG15, ρ, = 2.26 g/cm^3, particle size = 8.80 μm, surface area = 9.50 m^2/g, ash ≤ 0.100%, interlaminar distance = 0.3354–0.3358 nm). The ultrasonic bath used for the exfoliation is an Elma X-Tra 30H model with frequency of 35 kHz. Centrifugations to obtain the FLG were carried out with a benchtop Hettich ROTOFIX 32 A, with standard vessels. Solvents were dried and distilled using conventional methods. Column chromatography was carried out on silica gel (Merck Kieselgel 60, 230-240 mesh or Scharlau 60, 230–240 mesh). Thin-layer chromatography (TLC) was performed on aluminum sheets pre-coated with silica gel (Merck Kieselgel 60 F254). Vacuum filtrations were carried out with PCTE (pore size = 0.2 μm, Φ = 47 cm) and PTFE (pore size = 0.2 μm, Φ = 47 cm) membranes.

NMR spectra were recorded on a Bruker DPX-300 or a Bruker AVIII-700 at 298 K, using partially deuterated solvents as internal standards. Chemical shifts (δ) are expressed in ppm and are referred to the residual peak of the solvent. Spin multiplicities are reported as singlet (s), doublet (d), triplet (t) and multiplet (m), with proton-proton coupling constants (J) given in Hz. **Mass spectrometry** analyses were performed in the Mass Spectrometry Unit of the Universidad Complutense de Madrid. Electronic Impact measurements (EI) were recorded using a HP 5989A apparatus (70 eV, 200 °C). MALDI-TOF measurements were recorded utilizing a Brucker Ultraflex III apparatus. **IR** spectra were recorded on a Bruker TENSOR 27 (4000-370 cm^{-1}), with a resolution of 1 cm^{-1}. **UV-Vis-NIR** absorption spectra were done on a Shimadzu UV-3600, with a resolution of 1 nm. **Fluorescence** spectroscopy was performed in a Fluoromax-4 spectrofluorometer (HORIBA). UV and fluorescence titrations were performed by adding increasing amounts of graphene previously exfoliated in N-methylpyrrolidone (NMP) to a known concentration solution of **1** and **2**, all spectra were recorded at 298 K. **Thermogravimetric analyses (TGA)** were carried out with a thermobalance TA-TGA-Q-500 under air atmosphere. The sample (~ 0.5 mg) was introduced inside a platinum crucible and equilibrated at 90 °C followed by a 10 °C / min. ramp between 90 and 1000 °C. **Transmission electron microscopy (TEM)** analysis were performed on a JEOL JEM 2100, with an acceleration voltage of 200 kV equipped with a camera CCD ORIUS SC1000 (model 832) and the microanalysis were performed by XEDS (OXFORD INCA). The samples were dispersed in water and dropped onto a holey carbon copper grid (200 mesh), the solvent was removed in a vacuum oven during 48 h. **Raman** spectra were recorded on a NT-MDT in Via Microscope at room temperature using an exciting laser source of 532 nm. **XPS** analyses were performed on a SPECS GmbH (PHOIBOS 150 9MCD) spectrometer operating in the constant analyzer energy mode. A non-monochromatic aluminium X-ray source (1486.61 eV) was used with a power of 200 W and a voltage of 12 kV. Pass energies of 75 and 25 eV were used for acquiring both survey and high resolution spectra, respectively. Survey data were acquired from kinetic energies of 1487 - 400 eV with an energy step of 1 eV and 100 ms dwell time per point. The high-resolution scans were taken around the emission lines of interest with 0.1 eV steps and

100 ms dwell time per point. SpecsLab Version 2.48 software was used for spectrometer control and data handling. The semi-quantitative analyses were performed from the C 1s (284.3 eV) signal. The samples were introduced as pellets of 8 mm diameter. All **electrochemical** measurements were performed with a potentiostat Autolab PGSTAT128N (EcoChemie, NL) using the software package GPES 4.9 (General Purpose Elec. Experiments). For conventional three electrode experiments a homemade single compartment electrochemical cell was employed. Glassy carbon (GC) electrodes from CH Instruments were used as working electrodes and Pt wire as counter electrode. Specific calomel electrode (1M LiCl for organic media from Radiometer Analytical) and sodium saturated calomel electrode were used as reference electrodes for experiments in organic solvents and aqueous environment, respectively. Prior to the experiments all solutions were deoxygenated by bubbling nitrogen for 5 min. All experiments were carried out at room temperature.

Graphene Glassy Carbon (GC) electrode modification

GC electrodes were modified with graphene by 3 different strategies as follows:

- Graphene Oxide/Glassy Carbon electrode (GO/GC): was prepared by drop-casting 5 µL of the synthesized graphene oxide[6,7] onto a glassy carbon electrode and left to dry.
- Electrochemically Reduced Graphene Oxide /Glassy Carbon electrode (GO-ER/GC): was assembled by drop-casting 5 µL of the synthesized graphene oxide onto glassy carbon electrode and left to dry. Then, the electrode was immersed in a buffer solution of pH 5, 0.1 M acetic acid/potassium acetate, and 15 cyclic voltammetry scans were applied between 0 and −1.5 V at 50 mV/s. After the repetitive scans the electrode was rinsed with Milli-Q water and left to dry.[8]
- FLG/Glassy Carbon electrode (FLG/GC): was prepared by successive deposition of 5 drops (10 µL) of the synthesized FLG onto a glassy carbon electrode and left to dry in a vacuum desiccator. In this case, graphene was exfoliated (FLG) in dimethylformamide (DMF) following the procedure described later.

The electrodes modification (GC, GO/GC, GO-ER/GC and FLG/GC electrodes) with the exTTF derivatives was carried out by incubation during appropriate times (depending on the study) in tetrahydrofuran (THF) solutions of exTTF, **1** and **2** at different concentrations. After the adsorption process, the electrodes were rinsed with clean THF in order to remove the electroactive molecules non-direct adsorbed on the electrode surface.

The electrochemical measurements to determine the electroactive molecules electrode surface coverage were carried out in DMF 0.1 M in tetrabutylammonium perchlorate (TBAP).

Biosensor fabrication

A GO-ER/GC electrode functionalized with **1** by immersion during 15 h in a 0.36 mM **1**/THF solution was used to prepare the biosensor. 2.5 µL of a solution containing 12.1 U/µL of horseradish peroxidase (HRP) in a 0.1 M phosphate buffer solution (PBS, pH = 6.5) were deposited onto the **1**/GO-ER/GC electrode. After that, 2.5 µL of 2.5 % glutaraldehyde solution were added and let to dry in order to cross-link the HRP on the electrode surface.

Biosensor response to H_2O_2 was obtained by chronoamperometry at 0.0 V.

2. Synthetic procedures

Synthesis of 2-(3,3,3-tris(4-methoxyphenyl)-1-propynyl))-9,10-bis(1,3-dithiol-2-yliden)-9,10-dihydroanthracene (5)
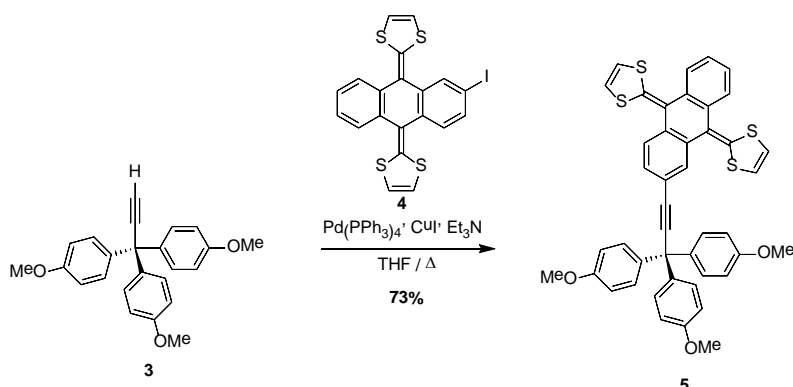
To a solution of 2-iodo-9,10-bis(1,3-dithiol-2-yliden)-9,10-dihydroanthracene **4**[4] (0.28 g, 0.56 mmol) in anhydrous THF (20 mL), 3,3,3-tris(4-methoxyphenyl)propine **3**[3] (0.100 g, 0.28 mmol), Pd(PPh$_3$)$_4$ (40%), CuI (40%) and Et$_3$N (0.12 mL, 0.84 mmol) were added. The reaction was refluxed under argon atmosphere overnight. After cooling to room temperature, AcOEt was added. The organic layer was washed with NH$_4$Cl solution (50 mL), water (2 x 50 mL) and NaCl solution (2 x 50 mL), and then dried with MgSO$_4$. The solvent was removed under reduced pressure and the crude was purified by silica gel column chromatography using an hexane/DCM (2/1) mixture as eluent. The final product was obtained as a yellow solid (151 mg, 73%).

^{1}H-NMR (300 MHz, CDCl$_3$), δ (ppm): 7.82 (d, 1H, J = 1.4 Hz), 7.73–7.60 (m, 3H), 7.40 (dd, 1H, J_1 = 8.0 Hz, J_2 = 1.4 Hz), 7.31–7.28 (m, 2H), 7.26–7.23 (m, 6H), 6.86–6.83 (m, 6H), 6.28 (s, 4H), 3.81 (s, 9H). ^{13}C-NMR (75 MHz, CDCl$_3$), δ (ppm): 158.7, 138.5, 136.9, 136.8, 135.8, 135.6, 135.4, 130.5, 129.5, 128.7, 128.3, 126.5, 125.4, 125.3, 122.2, 121.8, 121.6, 117.7, 113.7, 96.9, 85.2, 55.7, 54.6. FT-IR (CHCl$_3$), v (cm^{-1}): 2924, 2853, 1605, 1580, 1547, 1506, 1459, 1411, 1298, 1250, 1177, 1112, 1034, 828, 804, 757, 643, 588. UV-Vis (CHCl$_3$), λ_{max} (nm) (ε, M^{-1} cm^{-1}): 371 (19557), 438 (26937). MALDI-TOF-MS (m/z) calculated for C$_{44}$H$_{32}$O$_3$S$_4$ [M]$^+$: 736.1234, found: 736.1216.

Synthesis of 2-(3,3,3-tris(4-hydroxyphenyl)-1-propynyl))-9,10-bis(1,3-dithiol-2-yliden)-9,10-dihydroanthracene (6)
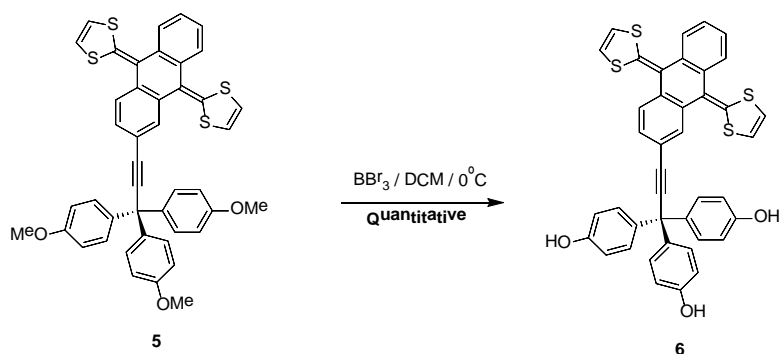

To a solution of **5** (0.1 g, 0.13 mmol) in anhydrous DCM (20 mL) at 0 °C and under argon atmosphere, BBr$_3$ (9.5 mL, 9.5 mmol) was added. The yellow solution turned brown

immediately. The reaction mixture was maintained under these conditions for 6 h. The reaction was worked up by addition of MeOH and H_2O. The precipitate was filtered under vacuum using a PTFE membrane. The final orange solid (90 mg) was employed without further purification in the next step assuming a quantitative yield.

^{1}H-NMR (300 MHz, Acetone-d_6), δ (ppm): 8.39 (s, 3H), 7.83 (d, 1H, J = 1.5 Hz), 7.72 (m, 3H), 7.48 (dd, 1H, J_1 = 8.0, J_2 =1.5 Hz), 7.37–7.34 (m, 2H), 7.15 (d, 6H, J = 8.7 Hz), 6.80 (d, 6H, J = 8.7 Hz), 6.62 (s, 2H), 6.61 (s, 2H). ^{13}C-NMR (75 MHz, Acetone-d_6), δ (ppm): 157.1, 138.3, 137.9, 136.6, 136.2, 130.9, 129.7, 128.6, 127.1, 126.1, 125.9, 122.2, 121.9, 121.5, 118.6, 115.5, 98.3, 85.1, 55.0. FT-IR (Acetone), v (cm^{-1}): 3360, 3064, 2960, 2922, 2851, 1701, 1600, 1549, 1509, 1456, 1411, 1367, 1260, 1228, 1170, 834, 802, 758, 650. UV-Vis (Acetone), λ_{max} (nm) (ε, M^{-1} cm^{-1}): 370 (6349), 435 (8348). MALDI-TOF-MS (m/z) calculated for $C_{41}H_{26}O_3S_4$ [M]$^+$: 694.0765, found: 695.0834 [M+H]$^+$.

Synthesis of 2-(3,3,3-tris(4-(4-(1-pyrenyl)butoxy)phenyl)-1-propynyl)-9,10-bis(1,3-dithiol-2-yliden)-9,10-dihydroanthracene (2)
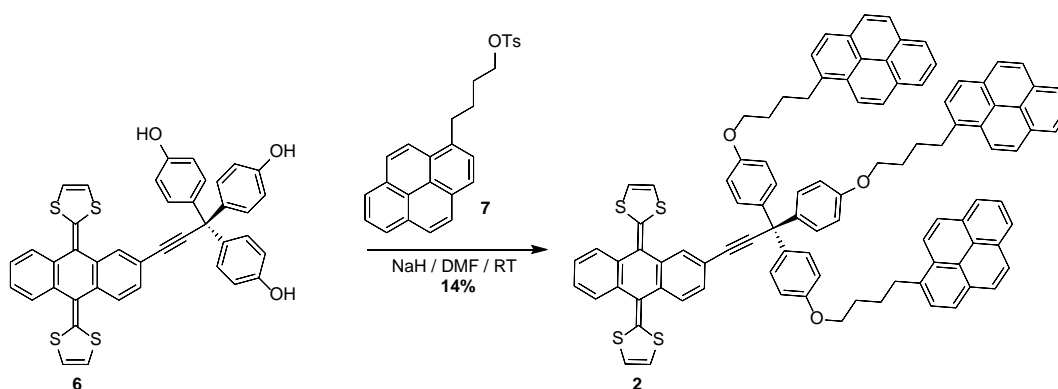
To a solution of **6** in dry DMF (0.095 g, 0.14 mmol, 4 mL) NaH (95%, 0.049 g, 2.05 mmol) was added slowly as a solid under argon atmosphere. The solution turned dark after the addition of the base. After two hours, a solution of 4-(1-pyrenyl)-1-butanol tosylate **7**[5] (0.26 g, 0.62 mmol) in 3 mL of dry DMF was added. The reaction mixture was stirred at room temperature overnight. TLC analysis of the mixture revealed that besides the expected triple nucleophilic substitution product, elimination of the tosylate group in **7** was also observed, as well as products of mono- and di-substitution. The solution was extracted with DCM and water. The organic layer was dried with Na_2SO_4 and the solvent was removed under reduced pressure. The residue was purified by silica gel column chromatography using initially hexane/AcOEt (4/1) and then changing to DCM/hexane (3/1). The final product was isolated as a yellow solid (29 mg, 14%).

^{1}H-NMR (700 MHz, CDCl$_3$), δ (ppm): 8.29 (d, 3H, J = 9.2 Hz), 8.18–7.96 (m, 21H), 7.89 (d, 3H, J = 7.7 Hz), 7.82 (d, 1H, J = 1.5 Hz), 7.71–7.61 (m, 3H), 7.40 (dd, 1H, J_1 = 7.9, J_2 = 1.5 Hz), 7.30–7.27 (m, 2H), 7.23 (d, 6H, J = 8.8 Hz), 6.83 (d, 6H, J = 8.8 Hz), 6.29 (s, 2H), 6.21 (s, 2H), 3.99 (t, 6H, J = 6.2 Hz), 3.39 (t, 6H, J = 7.7 Hz), 2.01 (m, 6H), 1.96–1.88 (m, 6H). ^{13}C-NMR (175 MHz, CDCl$_3$), δ (ppm): 157.8, 138.1, 136.6, 136.4, 135.3, 131.4, 130.9, 130.1, 129.8, 129.1, 128.6, 127.8, 127.5, 127.3, 126.6, 126.0, 125.8, 125.1, 125.0, 124.9,

124.8, 124.7, 123.4, 121.8, 121.3, 117.3, 117.0, 113.8, 96.6, 84.7, 67.7, 54.1, 33.2, 30.9, 29.3, 28.3. FT-IR (CHCl$_3$), v (cm^{-1}): 2955, 2920, 2853, 1728, 1604, 1546, 1506, 1464, 1379, 1288, 1246, 1173, 1119, 845, 763. UV-Vis (NMP), λ_{max} (nm) (ε, M^{-1} cm^{-1}): 315 (45787), 329 (91575), 345 (111355), 376 (20879), 445 (21978). MALDI-TOF-MS (m/z) calculated for C$_{101}$H$_{74}$O$_3$S$_4$ [M$^+$]: 1462.4521 found: 1462.4519.

Chemical exfoliation of graphene

Graphite (200 mg) was dispersed in NMP (100 mL) and sonicated at room temperature during 150 min., obtaining homogeneous aggregates. This dispersion was then centrifuged at 500 rpm for 45 min. After this process, the supernatant was isolated on vials with a Pasteur pipette. The graphene dispersion was kept in solution for further reactions.

Synthesis of supramolecular complex 1/FLG
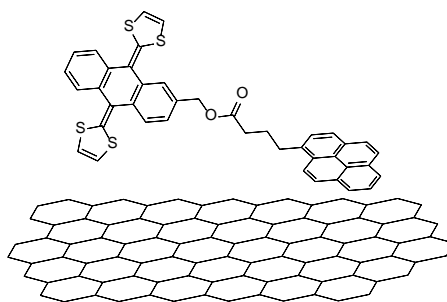
A sample of 4 mg of **1** was mixed with 20 mL of the graphene dispersion previously obtained in NMP. This mixture was sonicated during 30 min. After this time, the mixture was filtered on a PTFE membrane and washed with dichloromethane until the filtrate was transparent to afford the corresponding supramolecular complex.

FT-IR (KBr), v (cm^{-1}): 2957, 2924, 2855, 1736, 1702, 1585, 1458, 1385, 1113, 1049, 867, 804, 669.

TGA (air atmosphere): weight loss and desorption temperature (organic groups): 34.7%, 603 °C.

Raman: I$_D$/I$_G$ = 0.07.

UV-Vis (NMP), λ_{max} (nm): 329, 345, 432.

XPS: % atomic: C (284.6 eV) = 95.4, O (532.6 eV) = 4.47, S (163.6 eV) = 0.13.

Synthesis of supramolecular complex 2/FLG
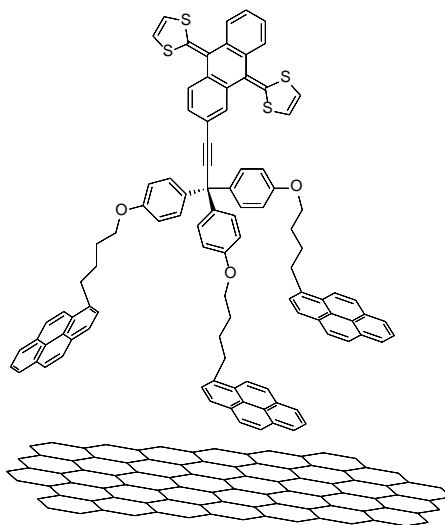
A sample of 7 mg of **2** was mixed with 20 mL of the graphene dispersion previously obtained in NMP. This mixture was sonicated during 30 min. After this time, the mixture was filtered on a PTFE membrane and washed with dichloromethane until the filtrate was transparent to afford the corresponding supramolecular complex.

FT-IR (KBr), v (cm^{-1}): 2956, 2925, 2854, 1740, 1682, 1582, 1455, 1434, 1385, 1214, 1157, 1034, 875, 772, 722, 667.

TGA (air atmosphere): weight loss and desorption temperature (organic groups): 31.6%, 628 °C.

Raman: I_D/I_G = 0.07.

UV-Vis (NMP), λ_{max} (nm): 329, 345.

XPS: % atomic: C (284.6 eV) = 90.12, O (533.6 eV) = 9.64, S (164.6 eV) = 0.23.

3. Characterization supplementary figures
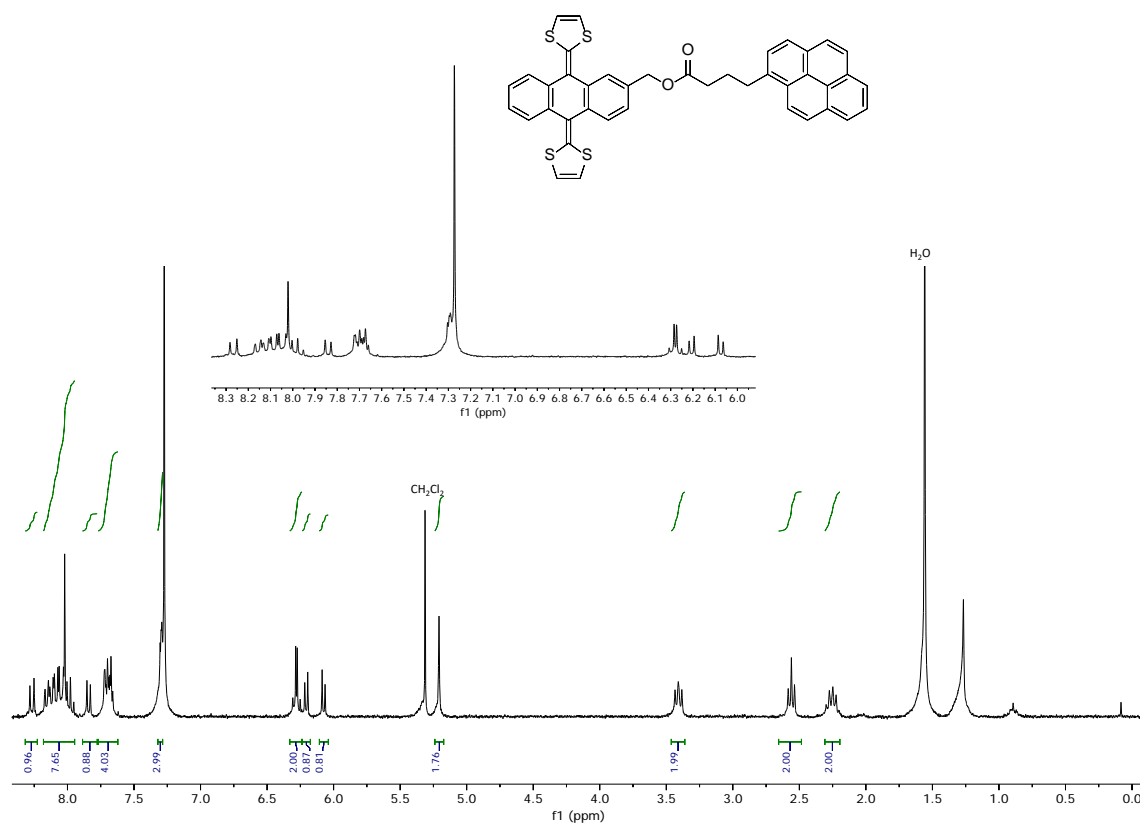
Fig. S1. ^{1}H-NMR of **1** (300 MHz, CDCl$_3$)
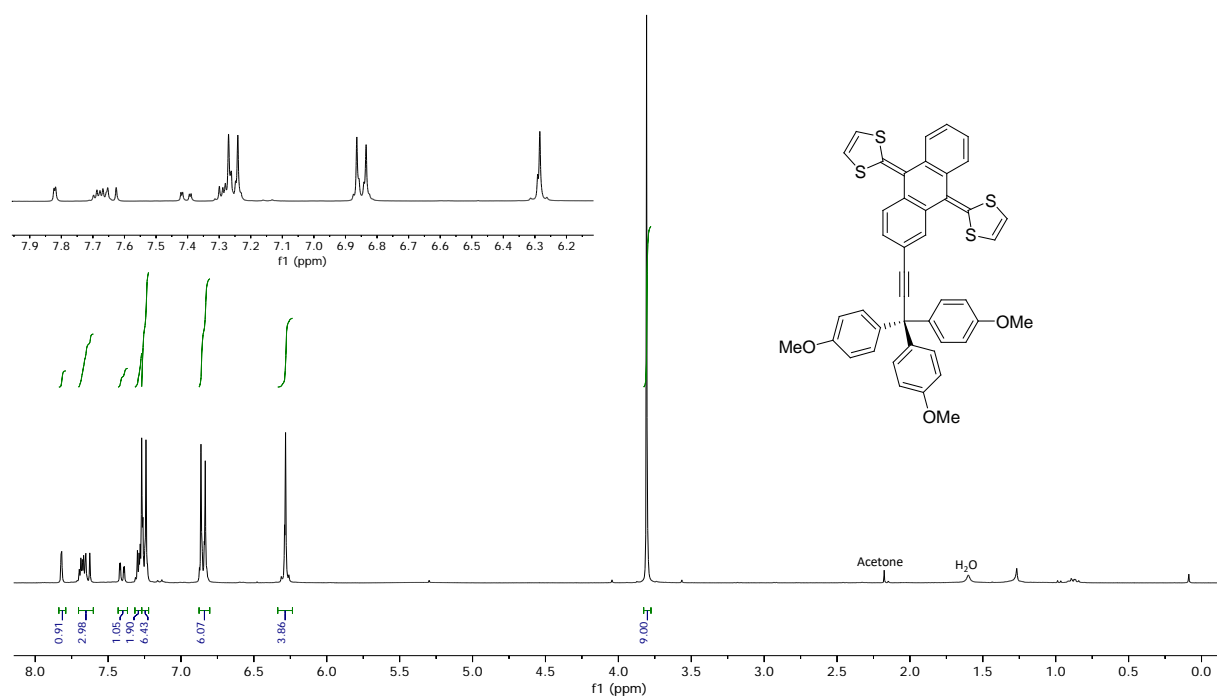
Fig. S2. ^{1}H-NMR of **5** (300 MHz, CDCl$_3$).
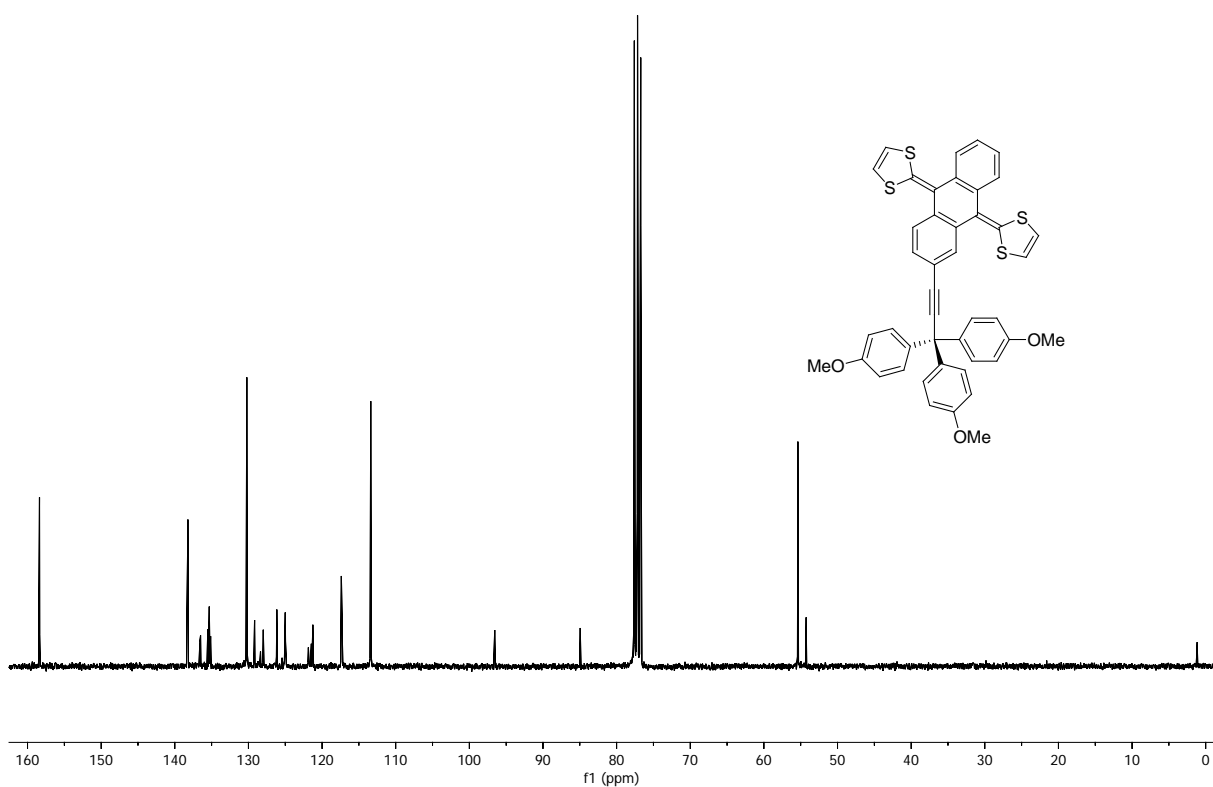
Fig. S3. ^{13}C-NMR of **5** (75 MHz, CDCl$_3$).
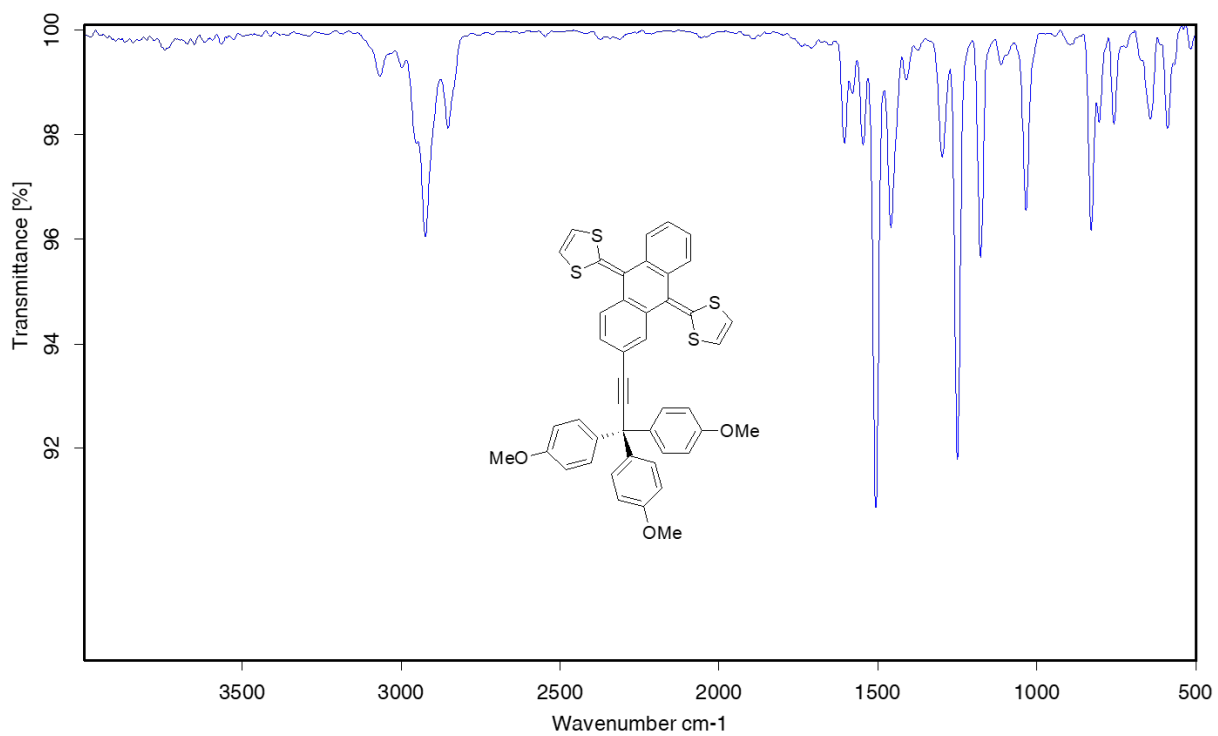
Fig. S4. FT-IR of **5**.
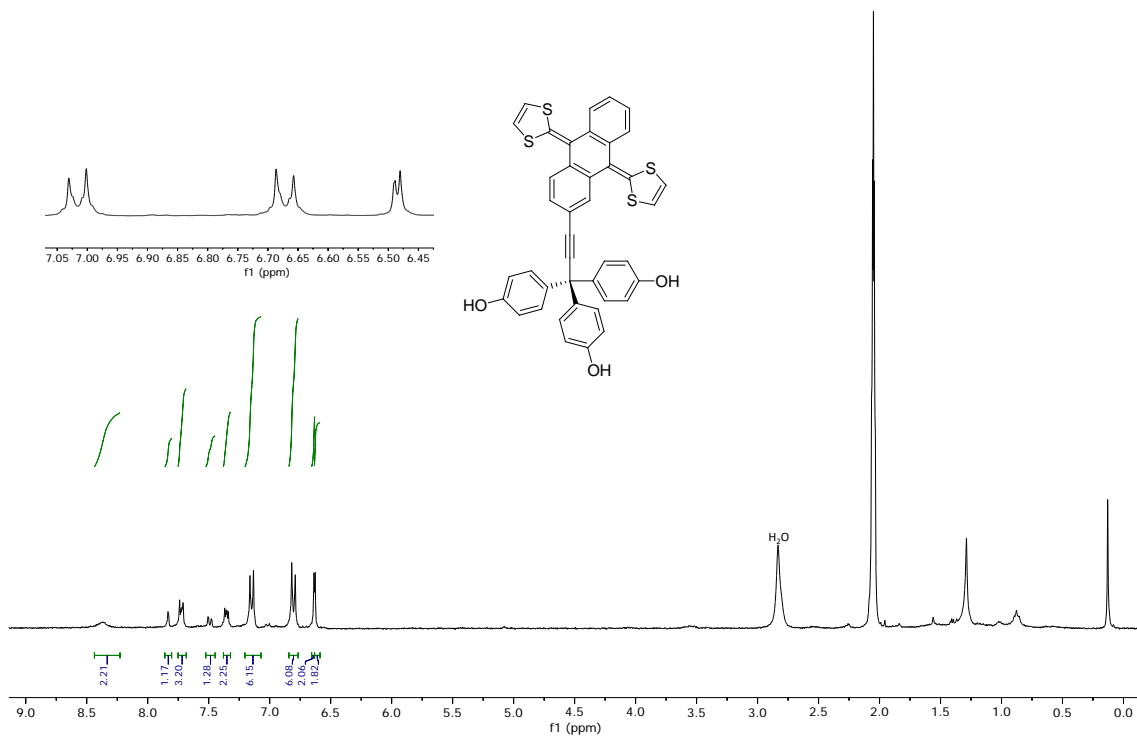
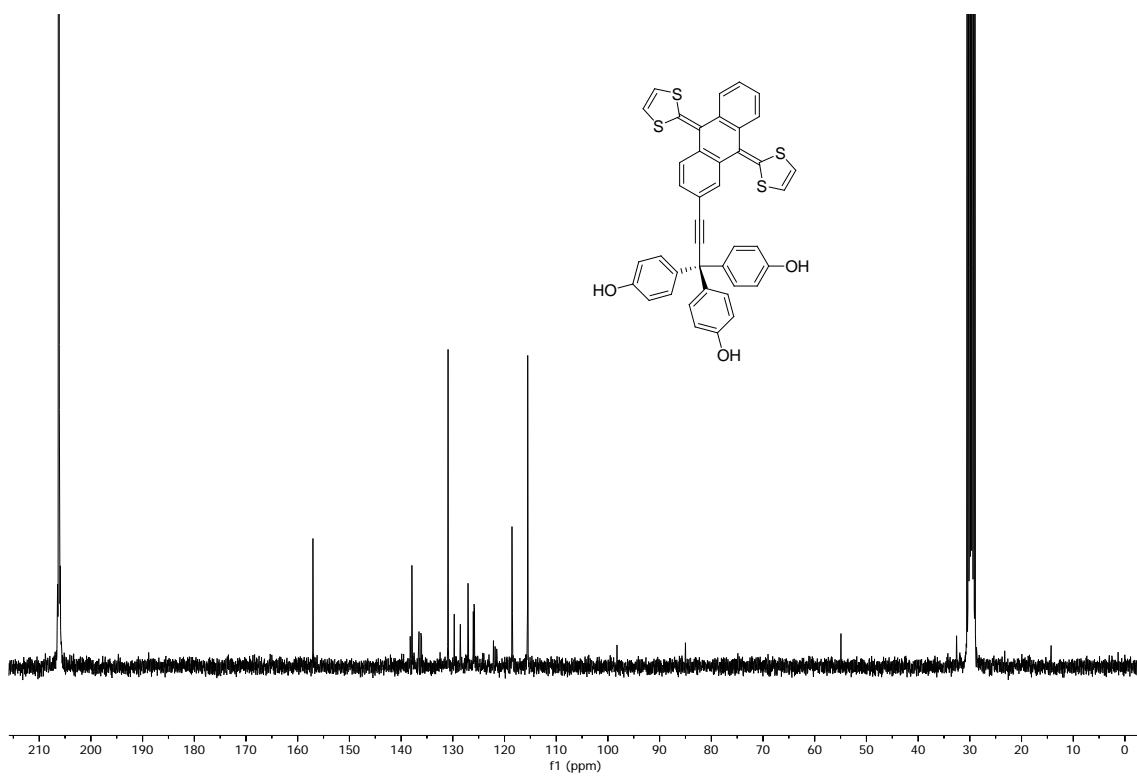**Fig. S5.** ^{1}H-NMR of **6** (300 MHz, Acetone-d_6).

Fig. S6. ^{13}C-NMR of **6** (75 MHz, Acetone-d_6).
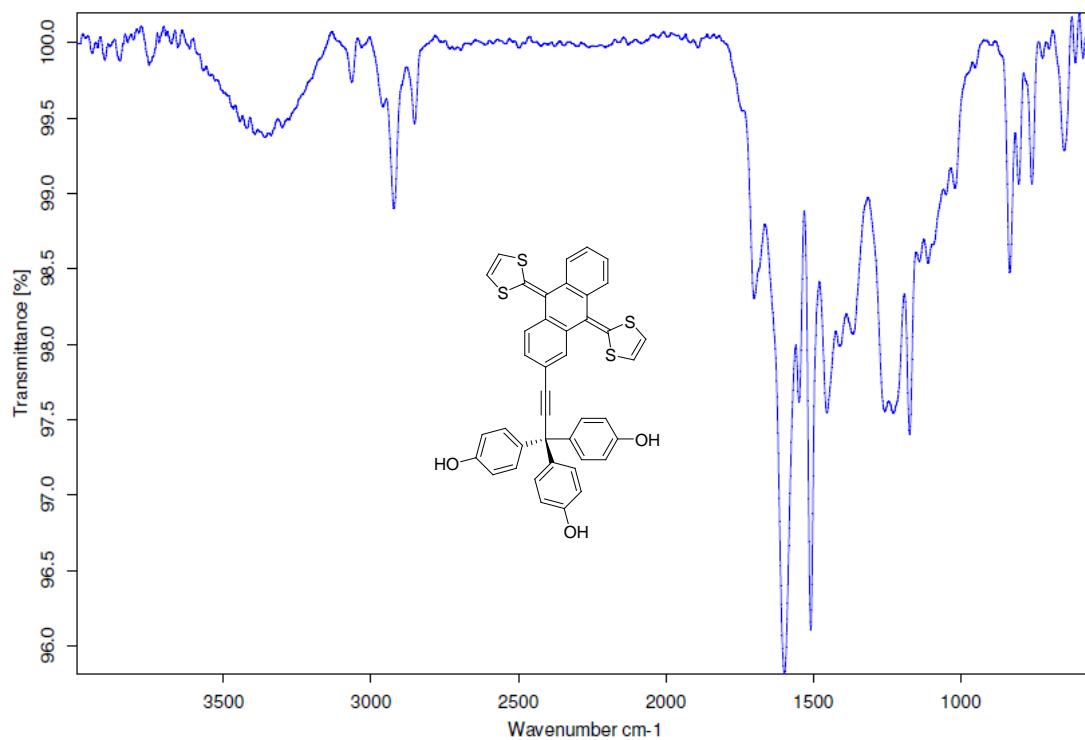
Fig. S7. FT-IR of **6**.
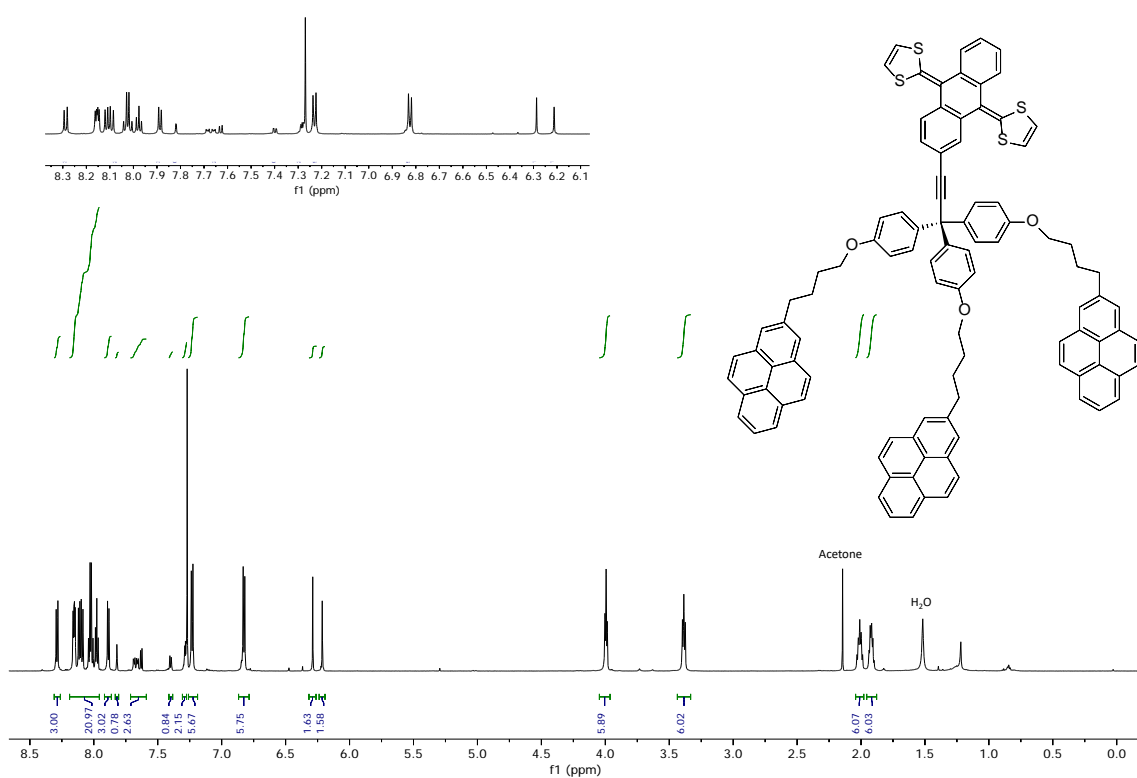
Fig. S8. ^{1}H-NMR of **2** (700 MHz, CDCl$_3$).
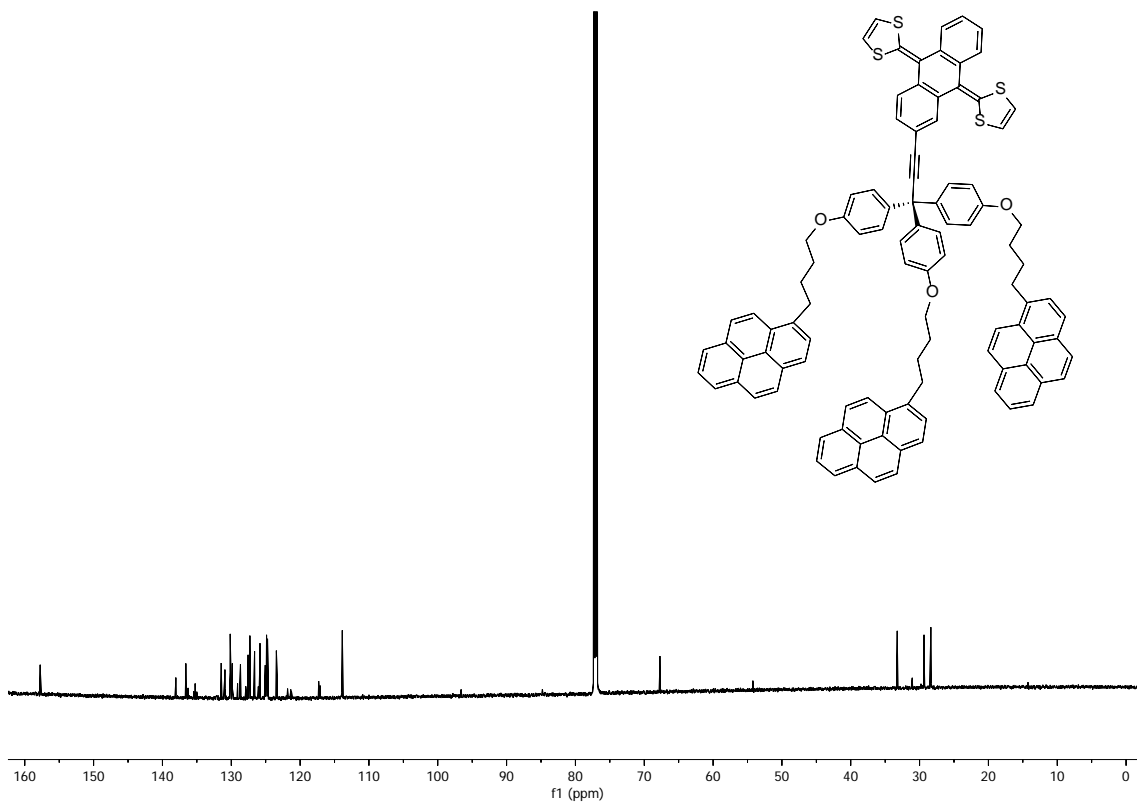
Fig. S9. ^{13}C-NMR of **2** (175 MHz, CDCl$_3$).
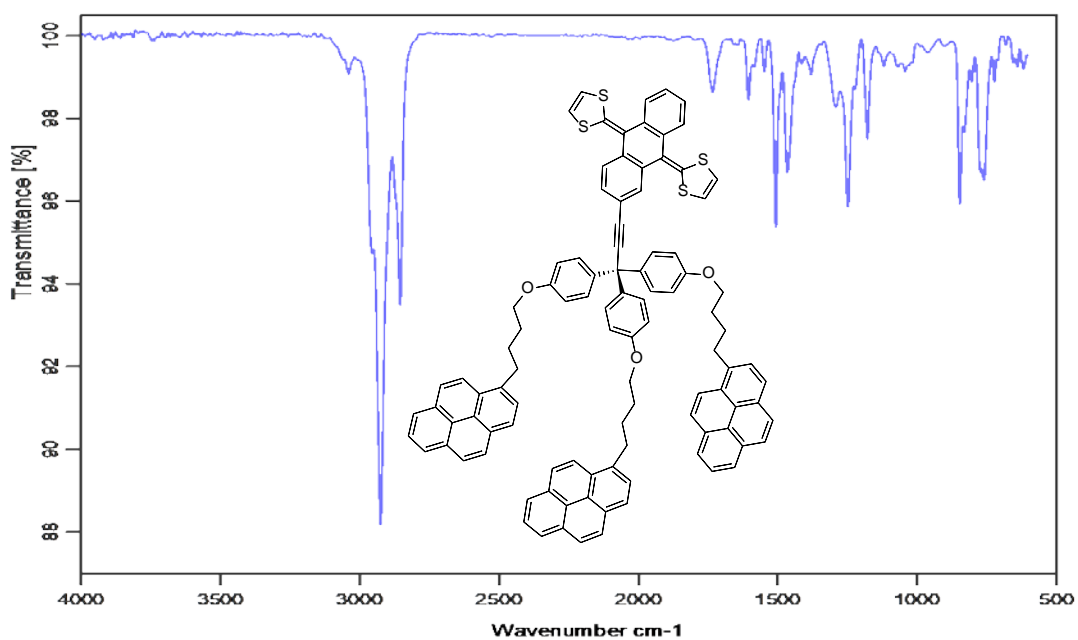
Fig. S10. FT-IR of **2**.

In order to confirm that all the changes observed in the titrations with the FLG dispersion were not due to dilution, control experiments were carried out by adding equal amounts of NMP without FLG to a solution of known concentration of the desired compound. The arrows point to the most significant spectral changes
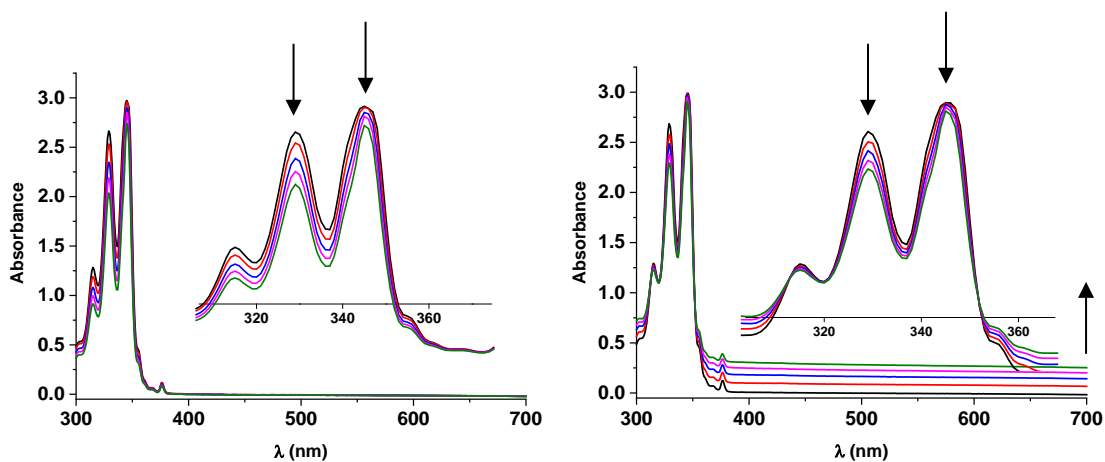

Fig. S11. UV-Vis absorption spectra of 4-(1-pyrenyl)-1-butanol (1.27×10^{-4} M) upon dilution with NMP (left) and titration with the FLG dispersion (right). Each addition corresponds to 100 µL.
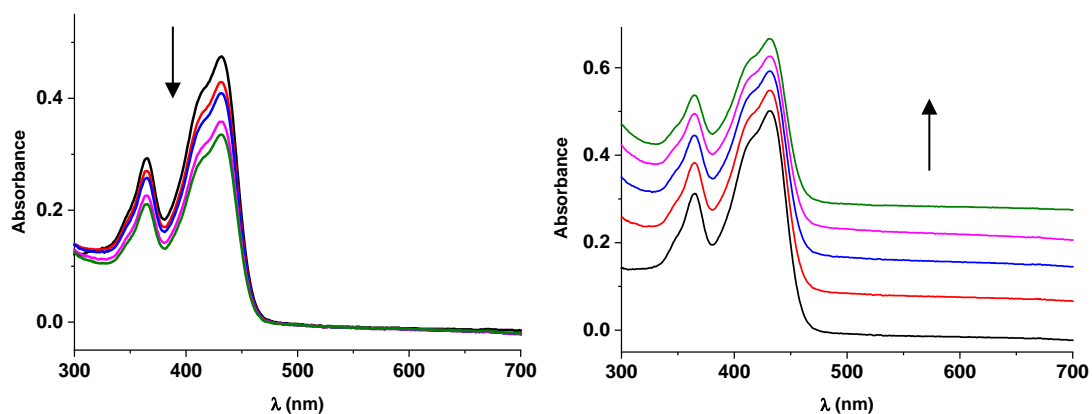

Fig. S12. UV-Vis absorption spectra of exTTF (3.94×10^{-5} M) upon dilution with NMP (left) and titration with the FLG dispersion (right). Each addition corresponds to 100 µL.
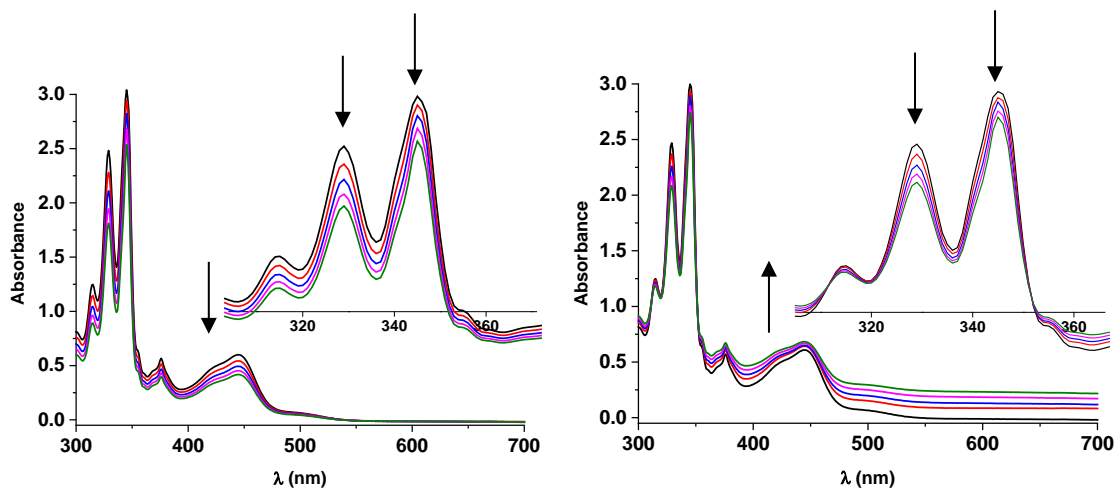
Fig. S13. UV-Vis absorption spectra of **2** (2.39 × 10⁻⁵ M) upon dilution with NMP (left) and titration with the FLG dispersion (right). Each addition corresponds to 100 μL.
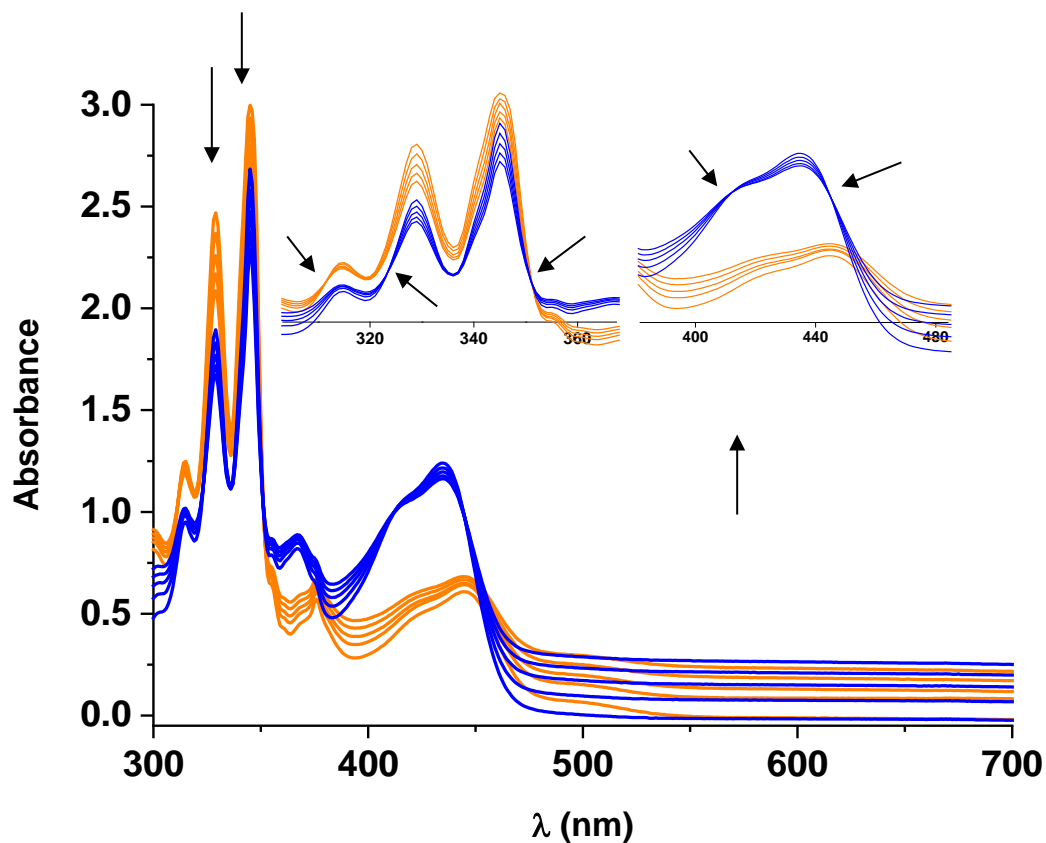

Fig. S14. Differences between the UV-Vis absorption spectra recorded for **1** (blue) and **2** (orange) upon titration with the FLG dispersion. In the inset graphs, the arrows spot the appearance of pseudo-isosbestic points upon FLG addition.

Regarding the emission spectra of **1** and **2** (Figs. S15 and S16), when comparing the titration experiment with the control one (dilution), an emission quenching, as the arrows point out, is noticed with the increasing addition of FLG, which suggests an interaction between FLG and the studied systems.
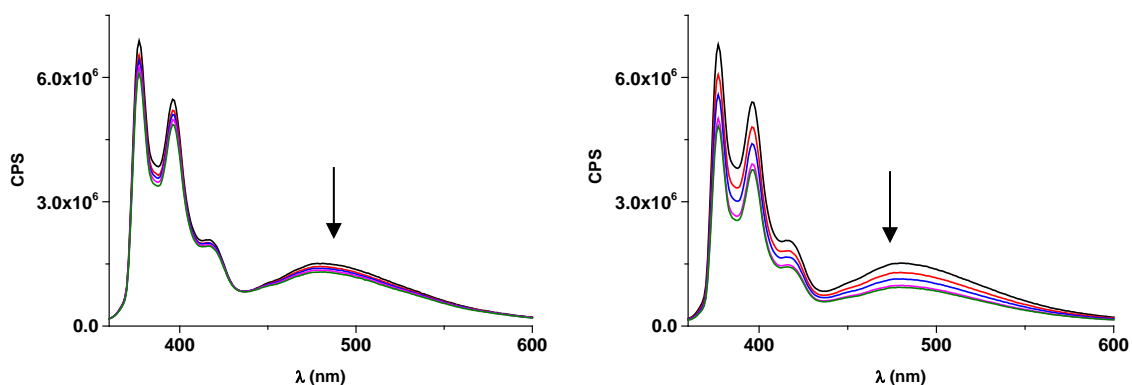
Fig. S15. Fluorescence spectra of **1** (2.94 × 10^{-5} M) obtained at λ_{exc} = 344 nm upon dilution with NMP (left) and titration with the FLG dispersion (right). Each addition corresponds to 100 µL.

Fig. S16. Fluorescence spectra of **2** (6.83 × 10^{-6} M) obtained at λ_{exc} = 344 nm upon dilution with NMP (left) and titration with the FLG dispersion (right). Each addition corresponds to 100 µL.
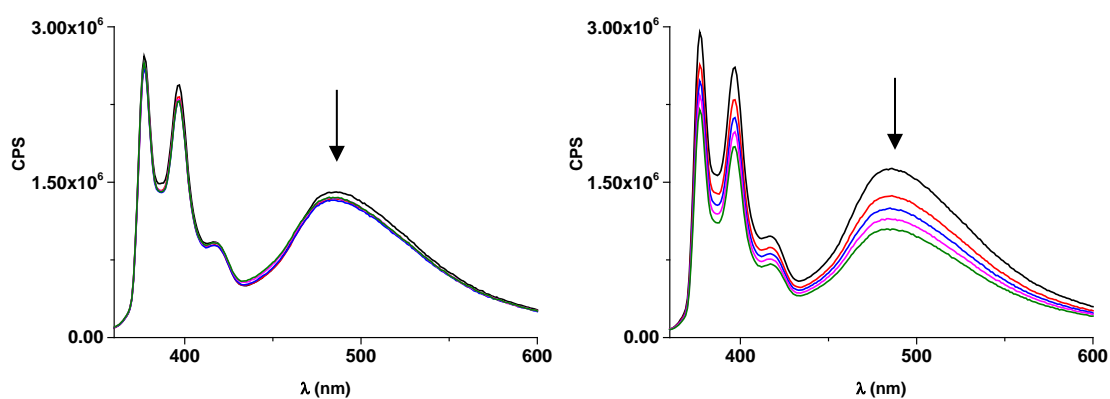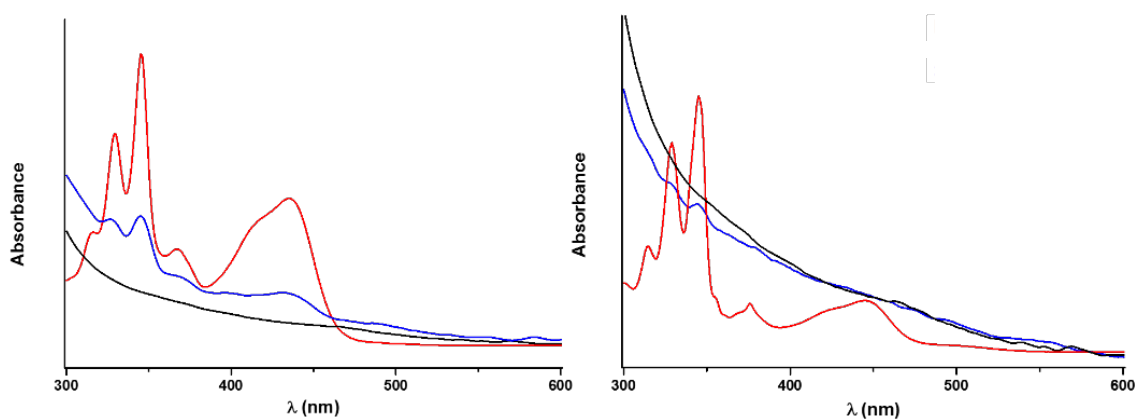

Fig. S17. Left: UV-Vis absorption spectra of FLG (black), **1** (red) and complex **1**/FLG (blue) in NMP. Right: UV-Vis absorption spectra of FLG (black), **2** (red) and complex **2**/FLG (blue) in NMP
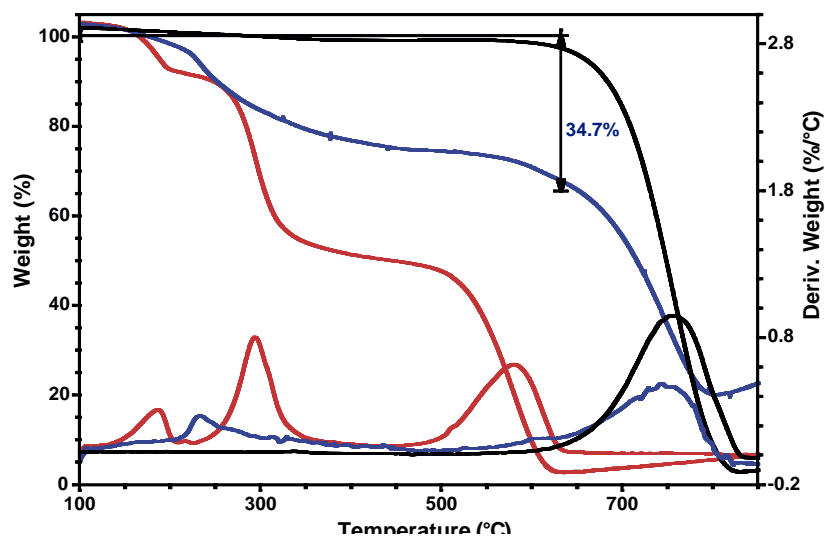
Fig. S18. TGA weight loss and first derivative curves recorded under air conditions for the exfoliated FLG (black) and the supramolecular complex **1**/FLG (blue), together with the thermal decomposition of **1** (red).
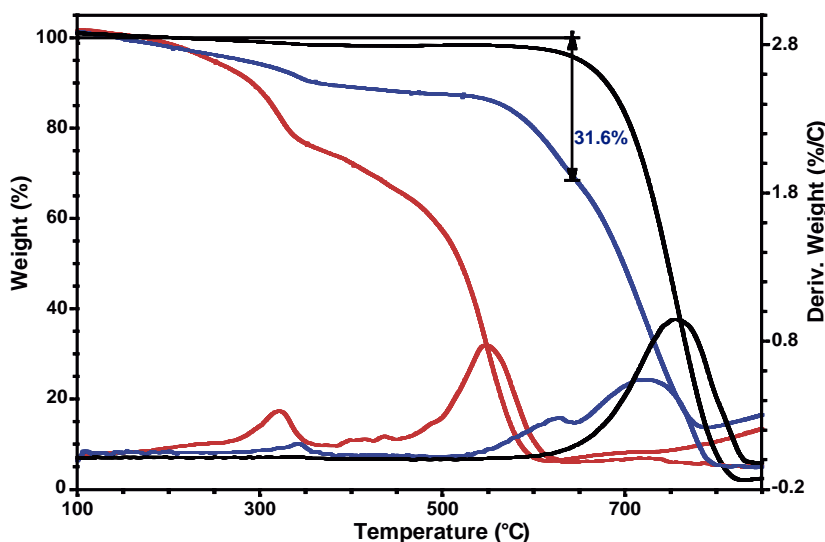

Fig. S19. TGA weight loss and first derivative curves recorded under air conditions for the exfoliated FLG (black) and the supramolecular complex **2**/FLG (blue), together with the thermal decomposition of **2** (red).
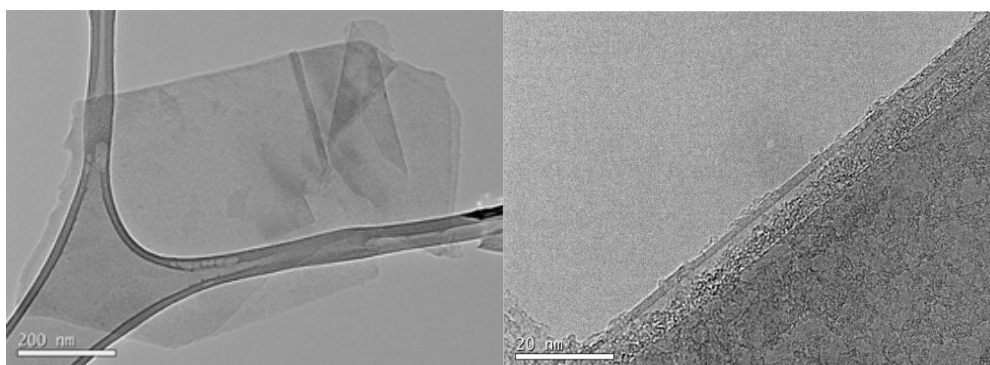
Fig. S20. TEM images of FLG obtained after the exfoliation procedure (left) and magnification where the graphene layers can be observed (right).
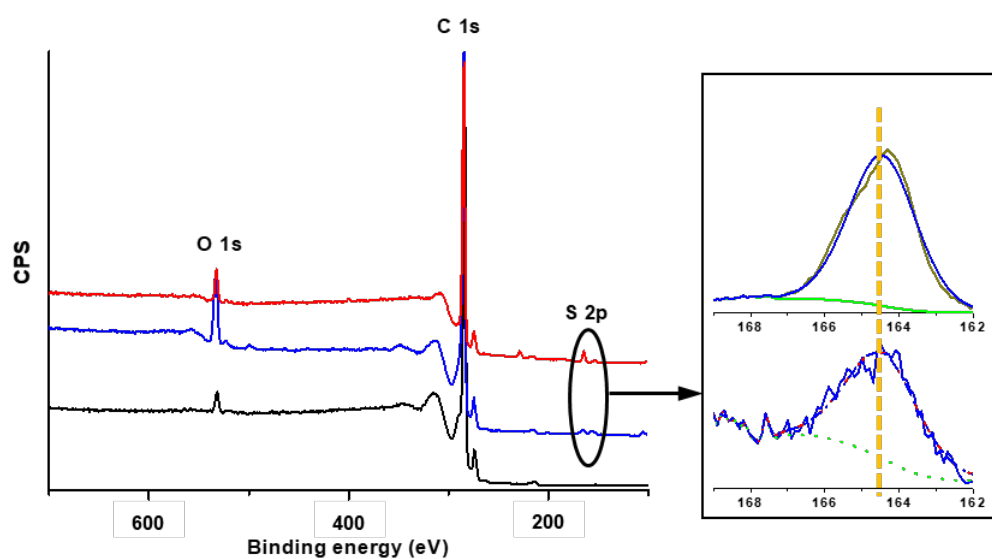

Fig. S21. XPS analysis of FLG (black), derivative **2** (red) and supramolecular complex **2**/FLG (blue). Detailed inset of the S 2p band of **2** (upper graph) compared to complex **2**/FLG (lower graph).

4. Theoretical calculations

Molecular dynamics simulations were performed using the NAMD software.[9] Initial geometries for the mono/tripodal assemblies of **1** and **2** with a graphene sheet were obtained with a minimization followed by a short dynamics simulation of 10 ns under a NVT ensemble at 298 K in gas phase. Then, molecular dynamics simulations in solution were performed including a box of explicit THF molecules as the organic solvent. The temperature and pressure were maintained at 298 K and 101.325 kPa (1 atm), respectively, by the Langevin thermostat and Langevin piston methods.[10] Non-bonded interactions were calculated using a scaled 1–4 protocol, in which all 1–3 pairs are excluded and all pairs that match the 1–4 criteria are modified. The electrostatic interactions for such pairs are modified by the constant factor defined by 1–4 scaling, in this case 1. The van-der-Waals interactions are modified by using the special 1–4 parameters defined in the parameter files. Local interaction distance common to both electrostatic and van der Waals calculations was set to 12 Å. A smooth switching function was applied to distances larger than 10 Å, and the distance between pairs for inclusion in pair lists was set to 14 Å. Electrostatic interactions were computed via the particle-mesh Ewald algorithm,[11] with a mesh spacing of < 0.12 nm. All chemical components of the simulations were represented in all-atom detail by CGenFF version 3.0.1.[12] The THF parameters were based on the CGenFF formulation.[13] The parameterization of the organic monopodal (**1**) and tripodal (**2**) receptors, and graphene, were assigned using the ParamChem web interface (CGenFF program version 1.0.0).[14]

The cubic box of THF was created by using the PackMol package[15] with dimensions $60 \times 60 \times 60$ Å^3. The initial solvent box contained 1604 molecules (20852 atoms) to match the density of THF (0.89 g/cm^3). The solvent box was minimized and equilibrated during a 10 ns NPT simulation (T = 298 K and P = 1 atm). A very small variation in the density of the simulated box from 0.87 to 0.90 g/cm^3 confirmed the reliability of the force-field. Then, a graphene sheet of 1002 atoms was soaked into the solvent box along with the desired organic molecule target of the interaction. The boundary threshold in the solute–solvent interaction was set to 2.4 Å. Long molecular dynamics simulations were carried out for the composite boxes under the NPT ensemble (T = 298 K and P = 1 atm), with a time step of 2 fs. Covalent bonds involving hydrogen atoms were constrained using the *rigidBonds* keyword. Simulations of 1×10^8 steps (simulation time = 200 ns) at least were calculated in all cases. Note that the coordinates of the graphene atoms were frozen along the MM/MD simulations for simplicity.

Figs. S22 and S23 summarize the evolution of the intermolecular distance between the reference exTTF and pyrene systems, respectively, and the graphene sheet along the dynamics simulation. Fig. S24 defines the inter and intramolecular geometry parameters analyzed along the dynamics for **1** and **2**. Figs. S25-S30 summarize the evolution of the characteristic geometry parameters defined in Fig. S24, and display representative snapshots of the MM/MD dynamics showing relevant conformational arrangements of the interaction between the organic monopodal/tripodal receptor and the carbon nanomaterial.

To shed light into the supramolecular recognition of the monopodal and tripodal pyrene-based derivatives by graphene, representative snapshots of the dynamics were extracted and optimized by means of the general MM3 force field[16] using Tinker 7.1[17] in vacuum and keeping the graphene atoms frozen. Pyrene-graphene and exTTF-graphene complexes were also modelled for comparison purposes. The interaction energy was estimated as the energy difference between the supramolecular nanohybrid and the constituting moieties at their miminum-energy geometry. Characteristic intermolecular geometry parameters for the nanohybrids (Fig. S31) were analyzed using the Chemcraft software[18] and visualized using the Chimera package[19].
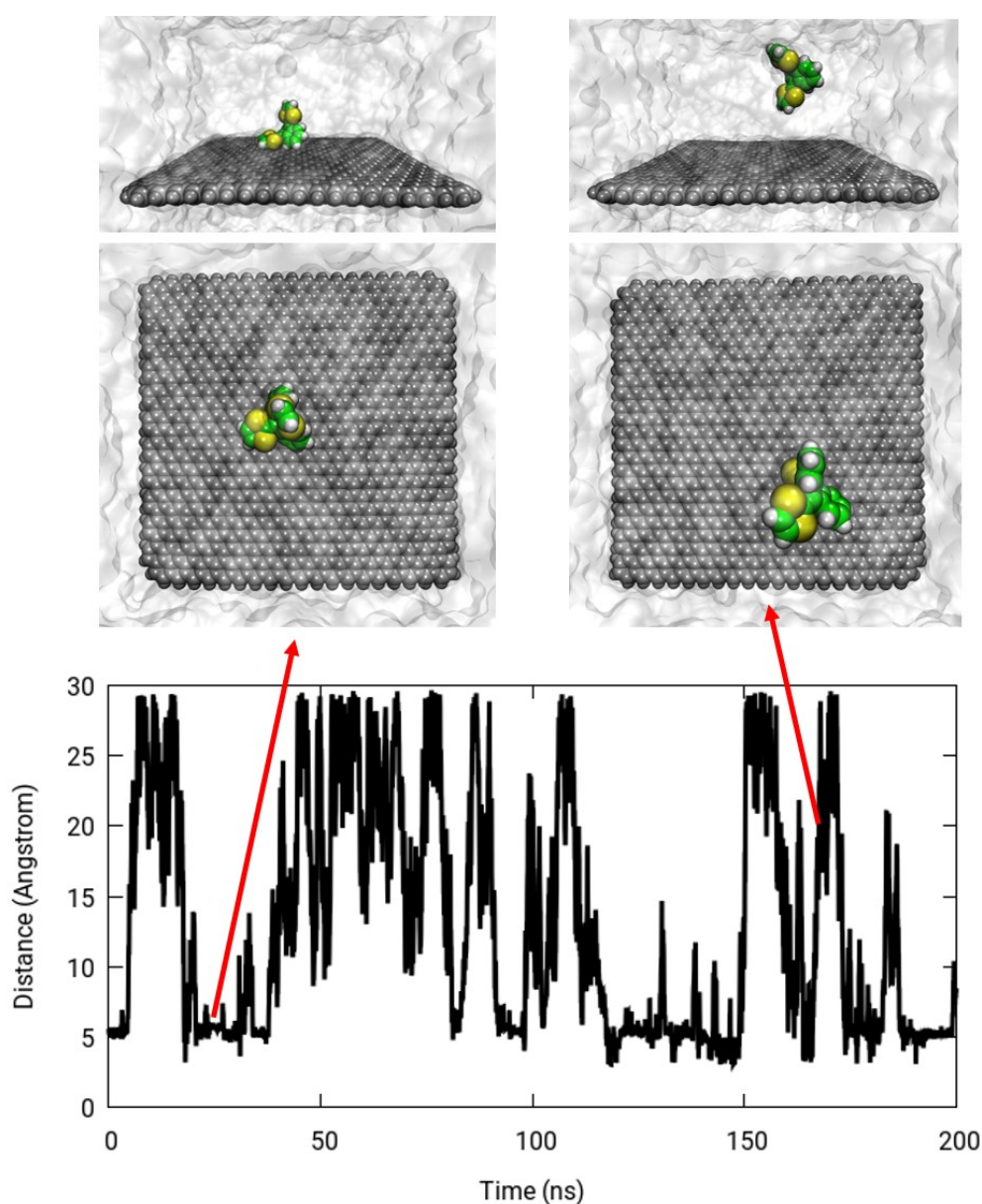

Fig. S22. Evolution of the intermolecular distance between the centroid of the exTTF molecule and the graphene sheet along the molecular dynamics simulation. Representative snapshots for adsorbed and desorbed exTTF configurations are displayed.
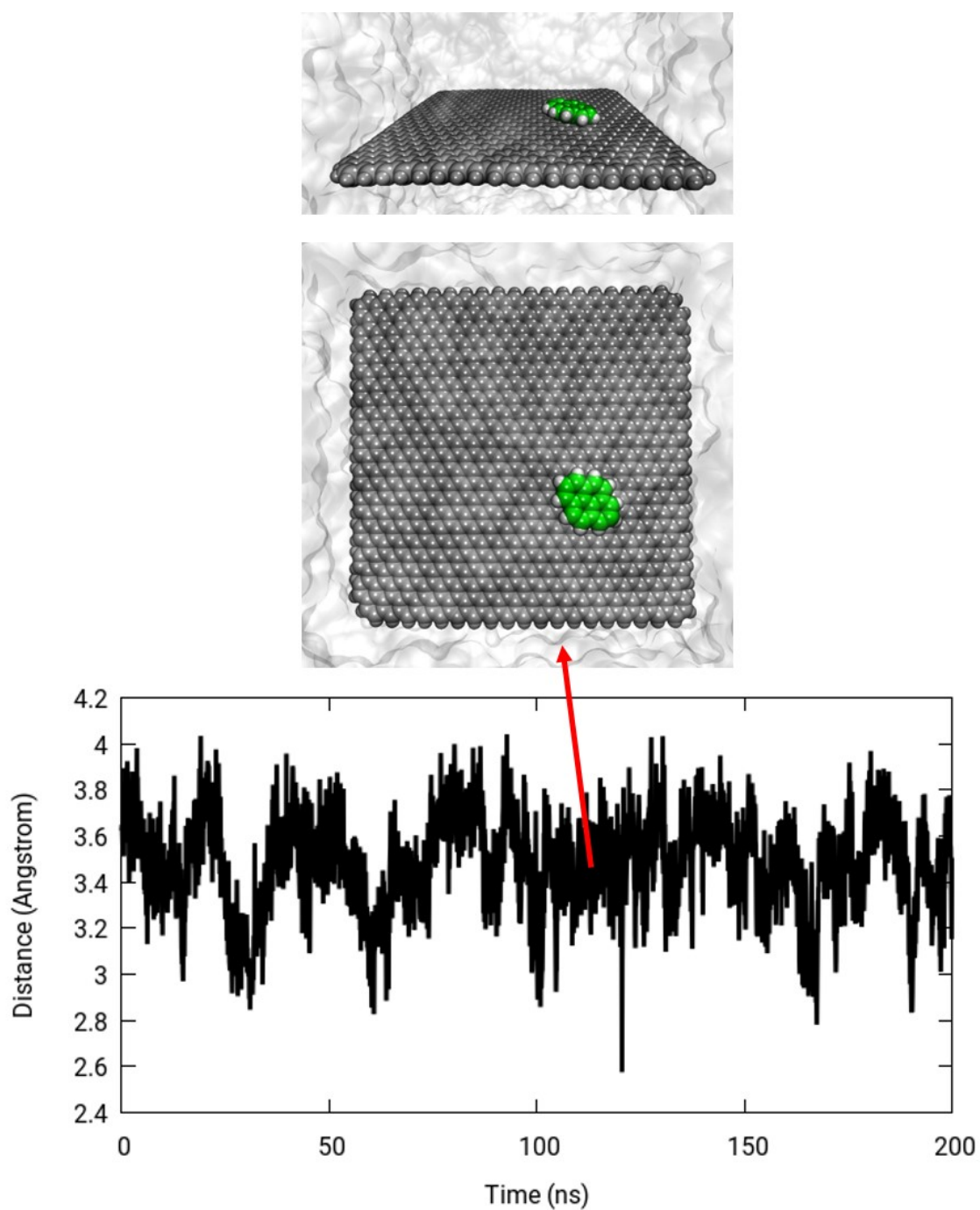
Fig. S23. Evolution of the intermolecular distance between the centroid of the pyrene molecule and the graphene sheet along the molecular dynamics simulation. A representative snapshot is displayed.
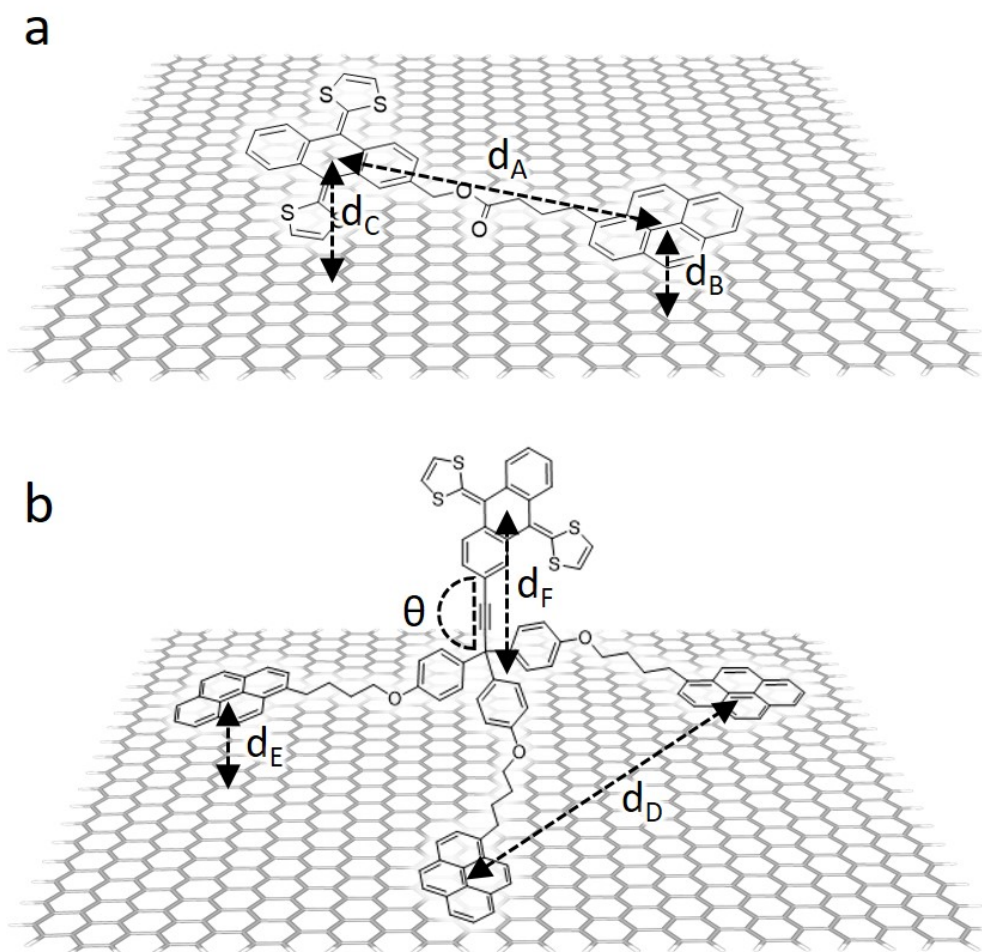
Fig. S24. Intra- and intermolecular geometry parameters used to characterize the disposition of **1** (a) and **2** (b) over a graphene sheet along the molecular dynamics simulations. For the monopodal nanohybrid **1**, d_A corresponds to the distance between the centroids of pyrene and exTTF moieties, d_B to the distance between the centroid of pyrene and the graphene surface, and d_C to the distance between the centroid of exTTF and the graphene surface. For tripodal nanohybrid **2**, d_D denotes the distance between the centroids of pyrene pairs, d_E the distance between the centroid of each pyrene and the graphene surface, and d_F the distance between the centroid of exTTF and the graphene surface. The tilting angle θ is defined as the angle between the sp^3 carbon connecting the three legs, the first sp carbon of the triple C≡C bond and the centroid of the exTTF head moiety.
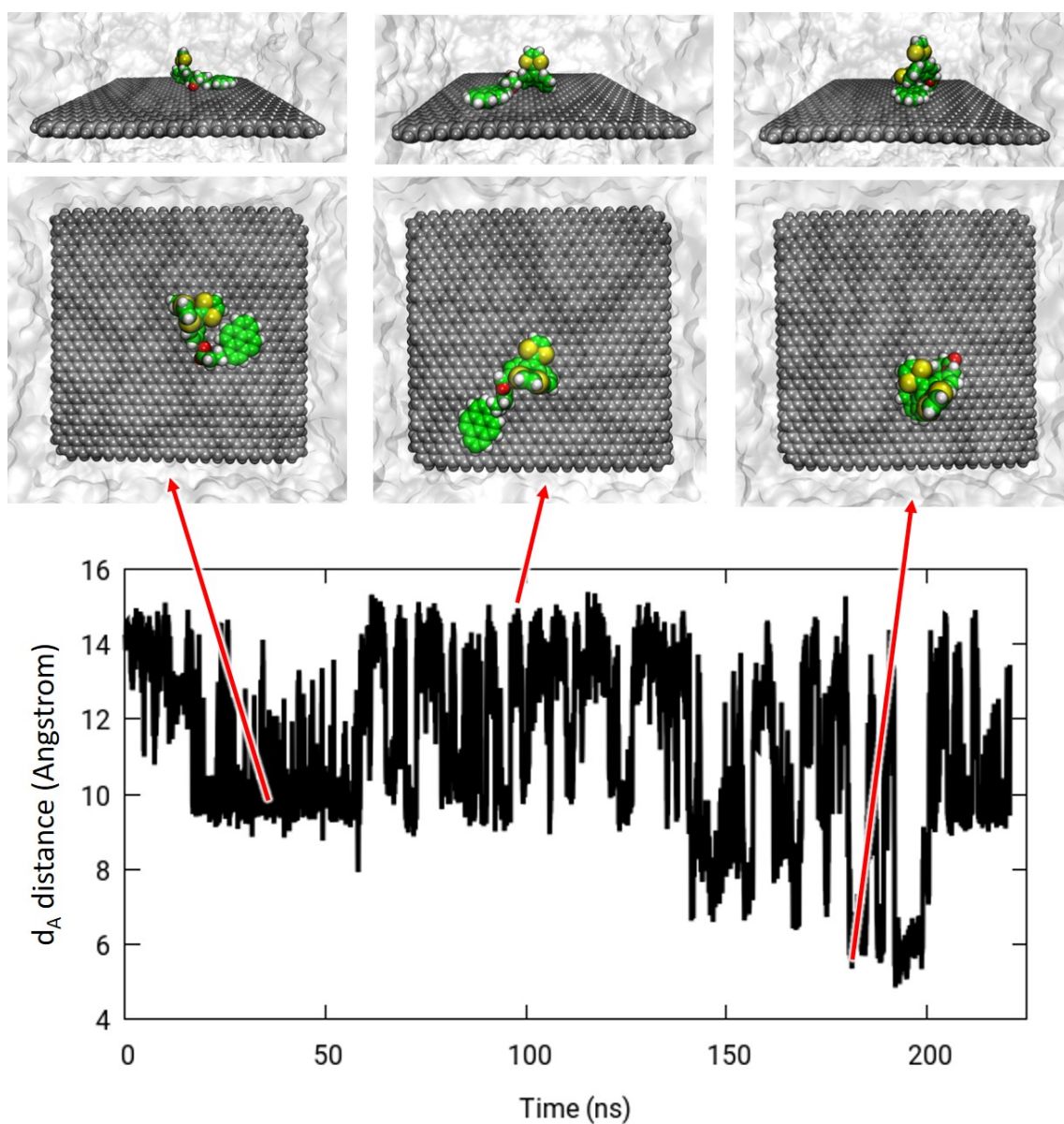
Fig. S25. Evolution of the intramolecular distance d_A between the centroids of pyrene and exTTF moieties (Fig. S24a) along the molecular dynamics simulation in the monopodal nanohybrid **1**. Representative snapshots with folded, unfolded and exTTF-detached conformations are displayed.
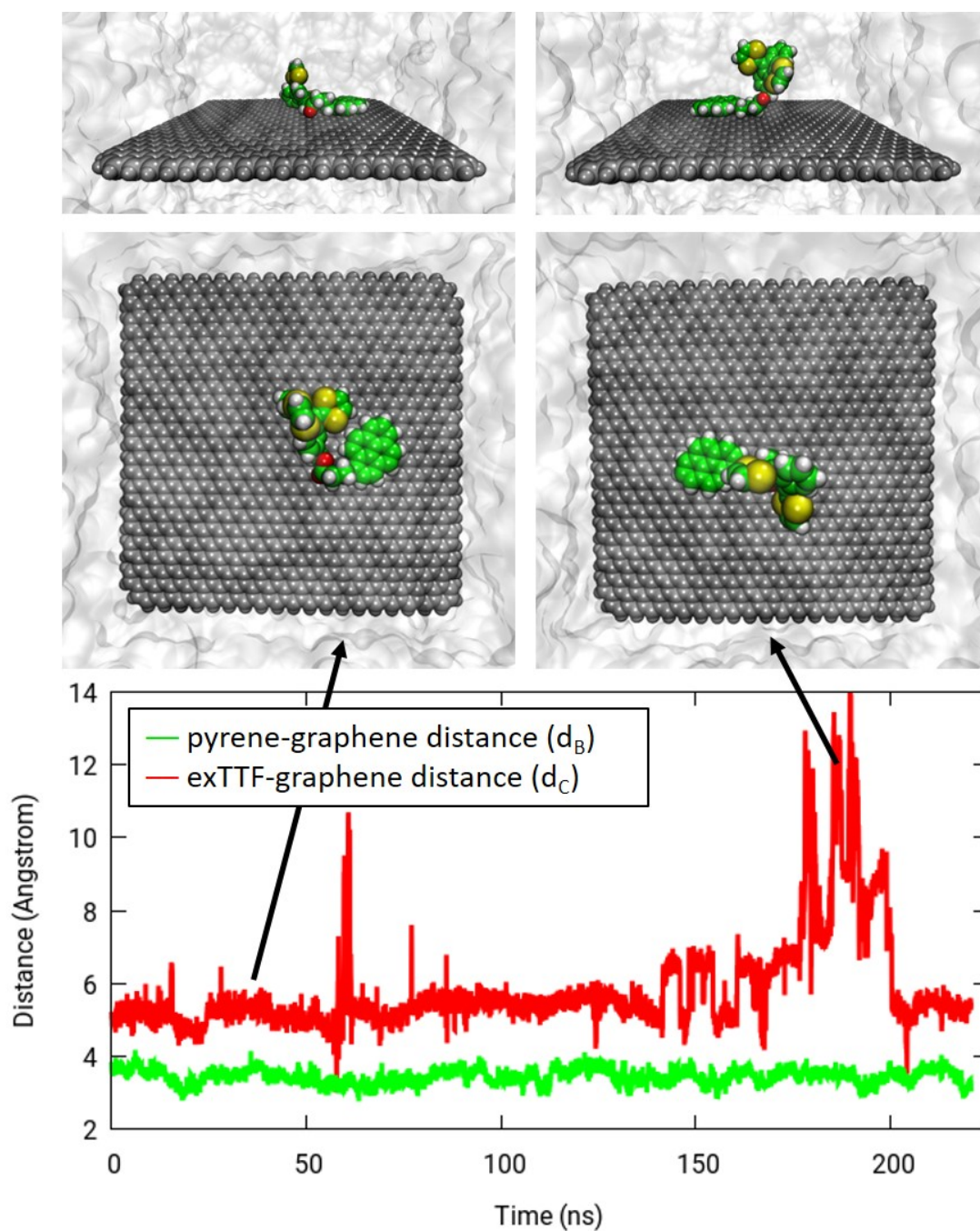
Fig. S26. Evolution of the intermolecular distances d_B and d_C between the centroids of pyrene or exTTF moieties and the graphene sheet (Fig. S24a) along the molecular dynamics simulation in the monopodal nanohybrid **1**. Representative snapshots with exTTF-attached and exTTF-detached conformations are displayed.
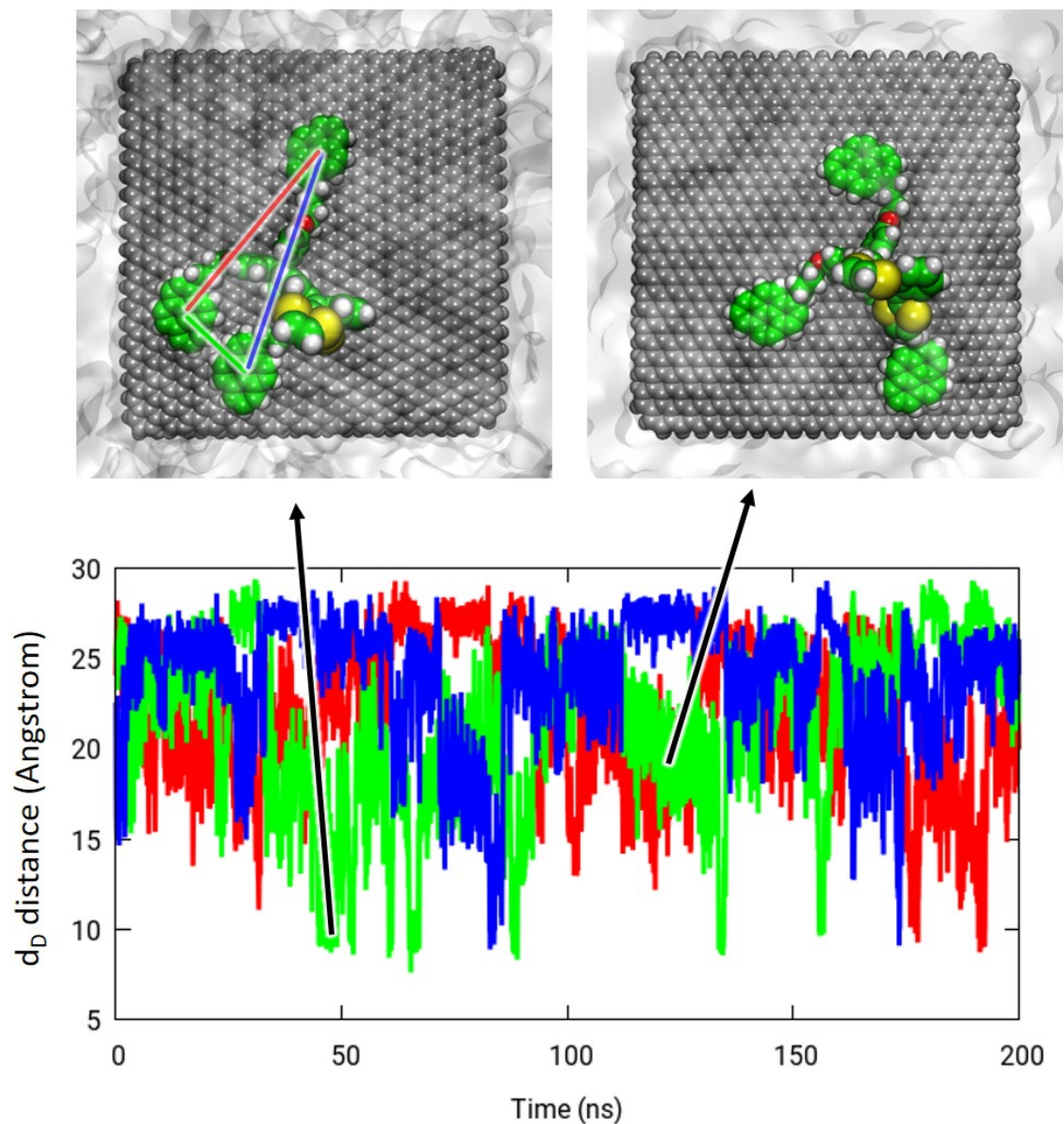
Fig. S27. Evolution of the intramolecular distance d_D between pyrene centroids (Fig. S24b) along the molecular dynamics simulation in the tripodal nanohybrid **2**. Representative snapshots with two interacting legs (top-left) and a fully extended conformation (top-right) are displayed.
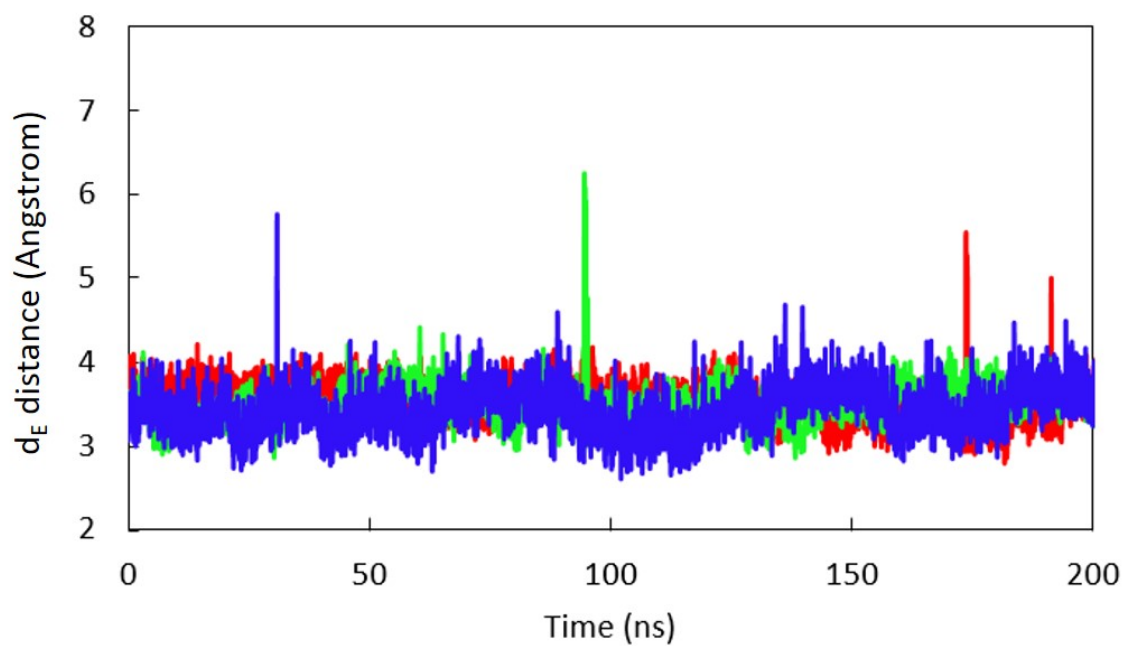
Fig. S28. Evolution of the intermolecular distance d_E between pyrene centroids and graphene sheet (Fig. S24b) along the molecular dynamics simulation in the tripodal nanohybrid **2**.
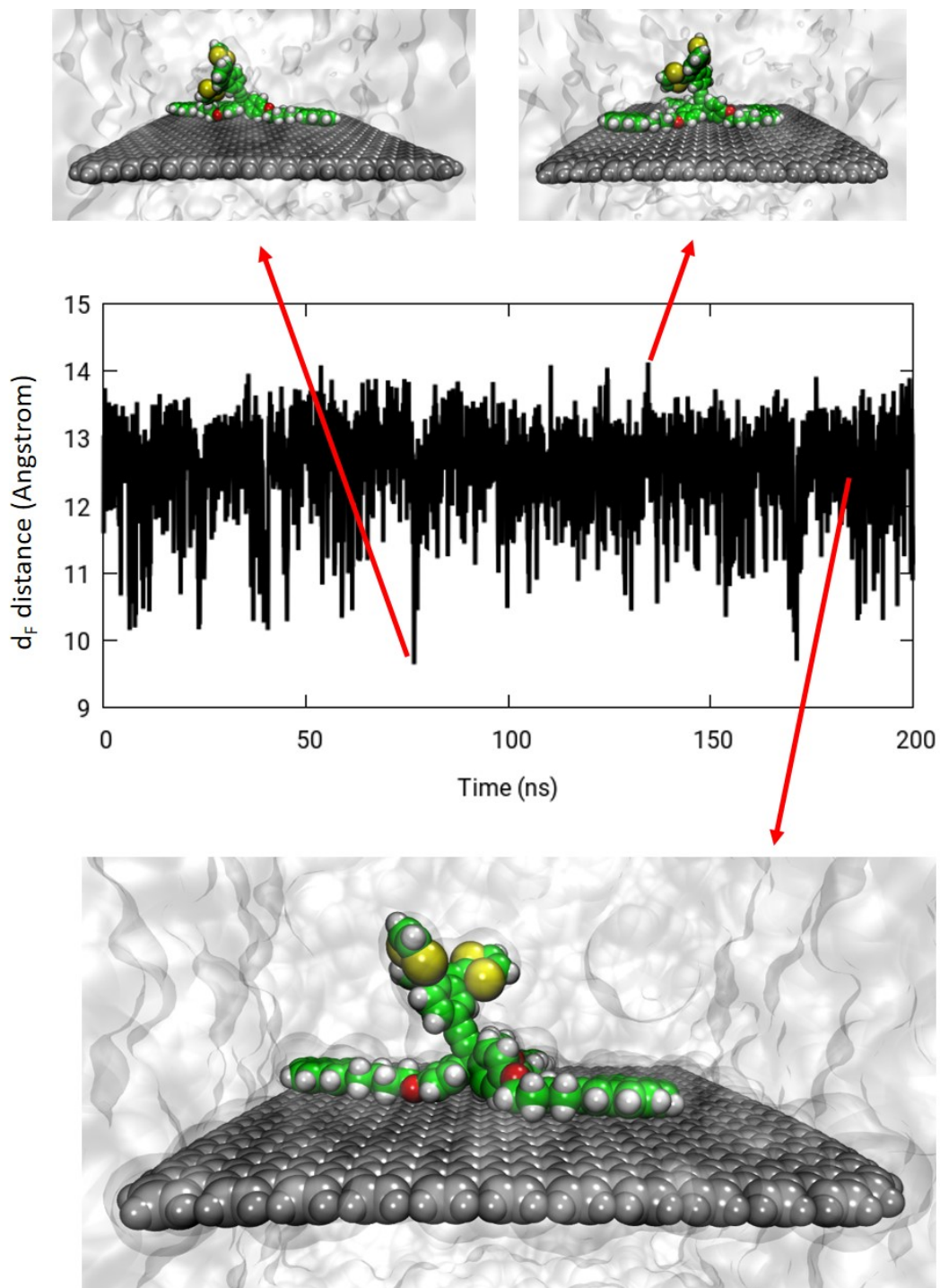
Fig. S29. Evolution of the intermolecular distance d_F (Fig. S23b) between the centroid of the exTTF unit and the graphene sheet (Fig. S24b) along the molecular dynamics simulation in the tripodal nanohybrid **2**. Representative snapshots with different exTTF-graphene separations are displayed.
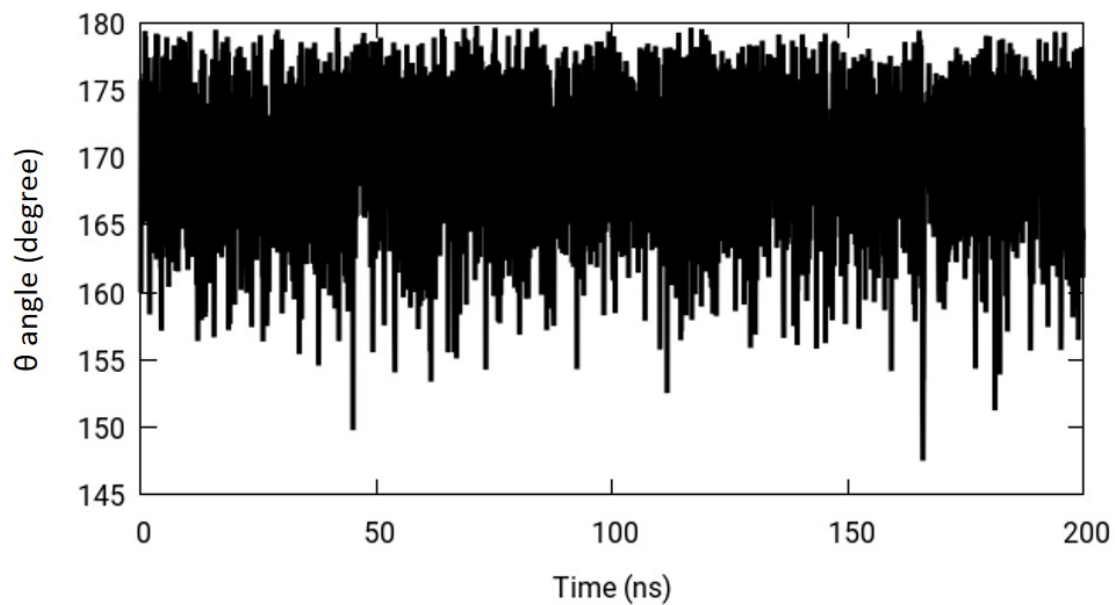
Fig. S30. Evolution of the tilting angle θ of the exTTF head moiety with respect to the triple C≡C bond (Fig. S24b) along the molecular dynamics simulation in the tripodal nanohybrid **2**.
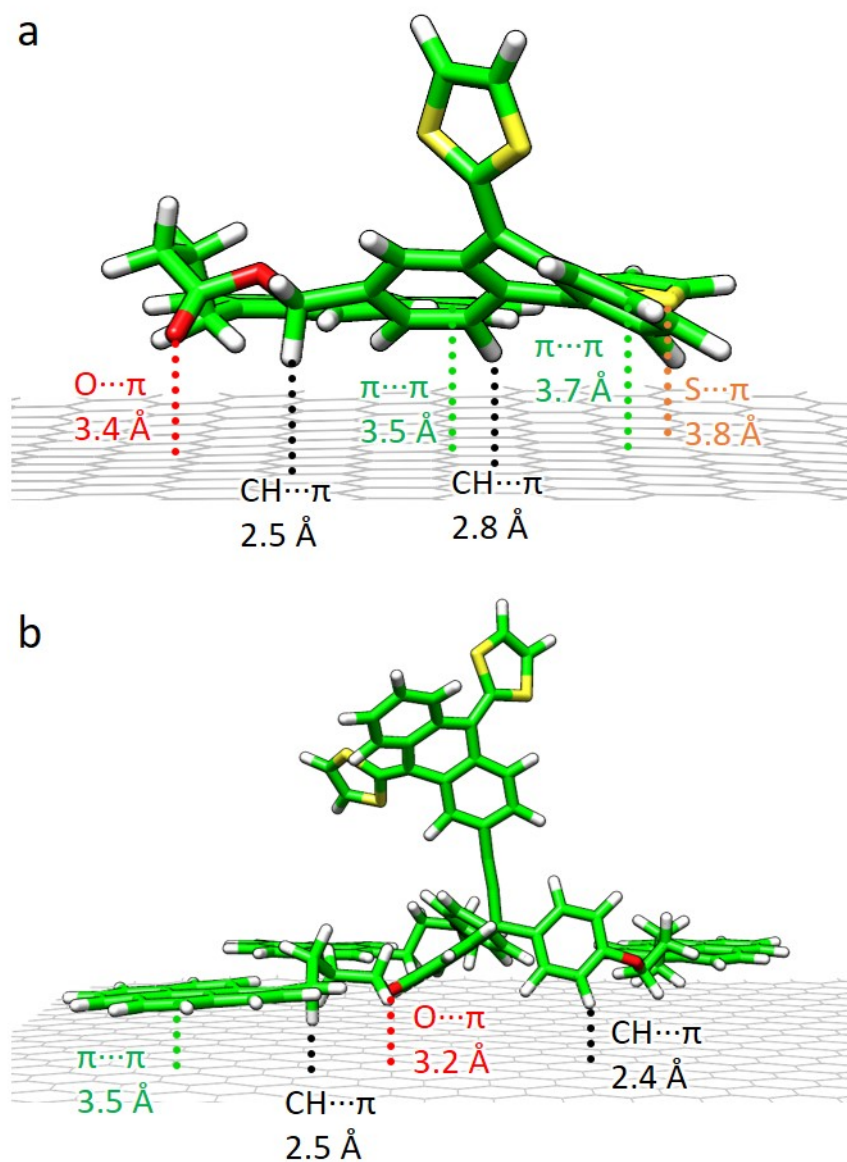
Fig. S31. Characteristic intermolecular distances indicating the noncovalent interactions that stabilize the supramolecular assembly of the exTTF-based nanohybrids in representative MM3-optimized structures of monopodal (a) and tripodal (b) complexes.

5. Electrochemical studies

Electrochemical behavior of 1 and 2 at graphene-modified electrodes

The electrochemical behavior of **1** and **2** at the different graphene-modified electrodes developed (GO/GC, GO-ER/GC and FLG /GC) was studied and compared to that obtained at unmodified GC electrode. The studies were carried out using 0.2 mM solutions of **1** or **2** in 0.1M TBAP/DMF. The first step was the GC electrode modification with the different types of graphene. Different amounts (2.5, 5 and 10 µL) of GO or FLG were drop-casted onto GC electrodes, in order to obtain a high and homogeneous surface coverage. In the case of GO-ER/GC, an electrochemical process was applied to reduce the GO. The response of these electrodes to redox probe (exTTF) was evaluated. The best results were obtained when 5 µL of GO or GO-ER were employed. When 10 µL of GO or GO-ER were used, a high current capacity and no faradaic process were detected, probably due to the thick layer of nanomaterial deposited. Based on these preliminary experiments, we decided to use 5 µL of GO in both electrode configurations (GO-ER/GC and GO/GC).

The cyclic voltammetric response of these graphene-modified electrodes to exTTF derivatives is shown in Fig. S32. In all cases, a redox couple appears around 0.3 V, which is ascribed to the oxidation of the exTTF moiety losing 2 electrons to the dication followed by the reduction of the oxidize form in the backward (reverse) scan.[20]

GO-ER/GC electrodes exhibit higher capacitive and faradaic currents compare to GO/GC electrodes. This feature indicates that the electrochemical reduction of GO generates a more conductive material (GO-ER) with better electron transfer than GO. This result is consistent with the loss of oxide groups from the GO surface after reduction, giving rise to a material with less defects and less oxide groups which interrupt the conduction band of the material.[21] FLG/GC electrodes show higher faradaic currents compared to GC electrodes and a slight increase on capacitive current. Both features are consistent with an increase in the conductivity and the electroactive area due to the nanomaterial.

Since these experiments were carried out with the electroactive molecules in solution, we expected that the voltammogram shapes correspond to diffusional processes. However, in the case of GO-ER-modified electrodes, the shape is the typical of a surface-confined redox process, which indicates that the adsorption of the electroactive molecule occurs. In the case of GC, GO and FLG, this process is less favored owing to the more unlikely π–π interactions due to the nature of the nanostructure. These results indicate that in the reduction process the oxide groups present on the GO surface, which could interrupt the conduction band of the material, are removed.
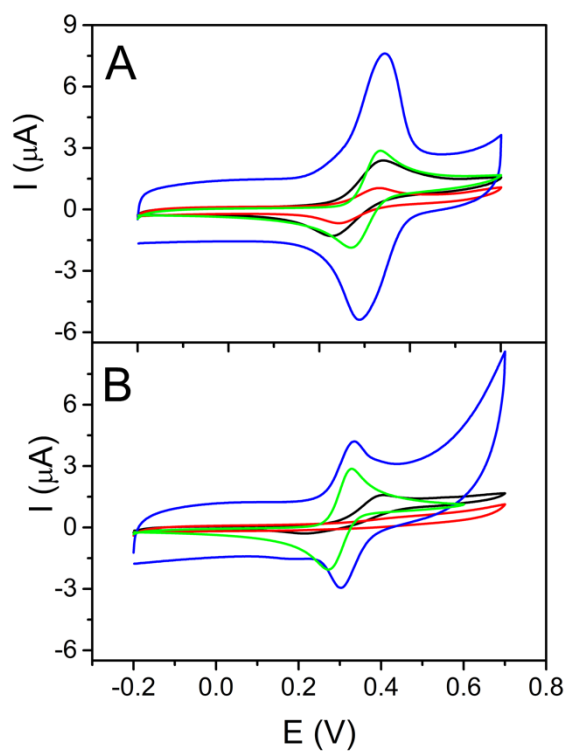
Fig. S32. Cyclic voltammograms of GC (black), GO/GC (red), GO-ER/GC (blue) and FLG/GC (green) electrodes immersed in 0.2 mM of (A) **1** or (B) **2** solutions in 0.1M TBAP/DMF at 10 mV/s.

Table S1. Differential potential peak (ΔE_p, mV) of voltammograms of GC, GO/GC, GO-ER/GC and FLG/GC in 0.2 mM of **1** or **2** solutions in 0.1M TBAP/DMF.

Electrodes	ΔE_p **1**	ΔE_p **2**
GC	112	198
GO/GC	92	282
GO-ER/GC	57	30
FLG/GC	58	54

Electrochemical behavior of 1 or 2 modified electrodes

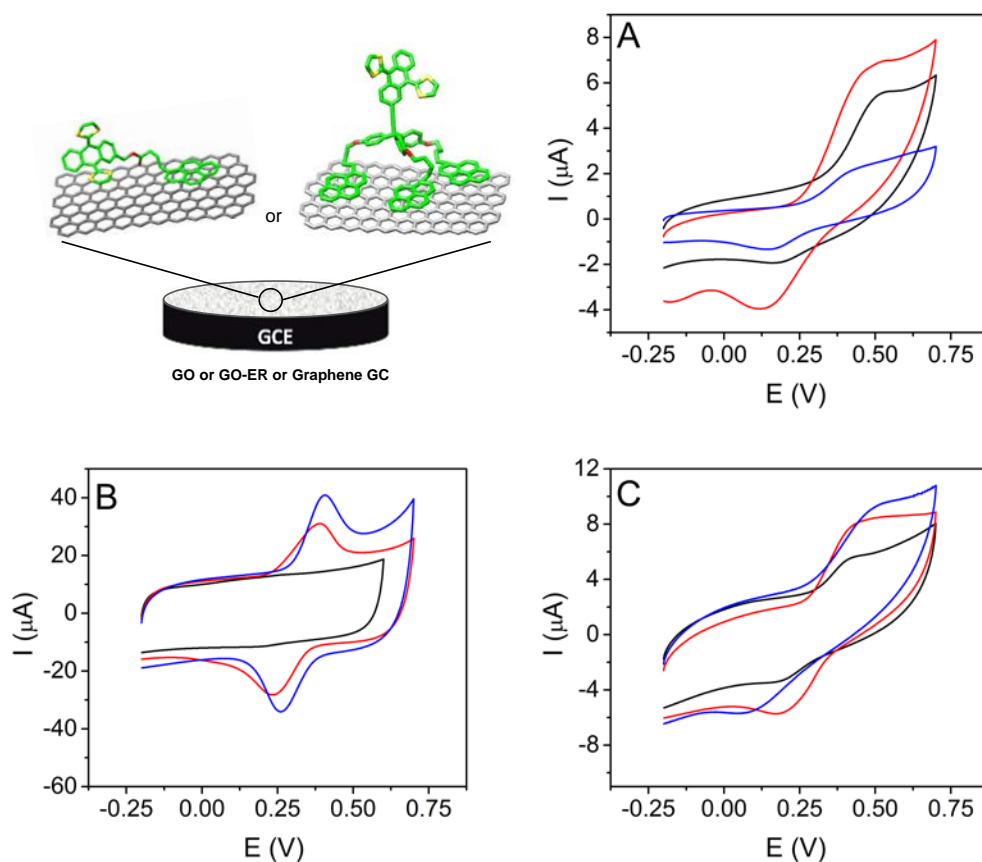**Fig. S33.** Schematic representation of the modified electrodes. Cyclic voltammograms of (A) GO/GC, (B) GO-ER/GC and (C) FLG/GC modified with exTTF (black), **1** (red) and **2** (blue) in 0.1 M TBAP/DMF at 100 mV/s.

Table S2. Heterogeneous charge transfer rate constant (k^o), transfer coefficient (α) and differential peak potential (ΔE_p) of **1** and **2** adsorbed onto different electrodes in 0.1 M TBAP/DMF.

Modified electrode	k^o (s^{-1})	α	ΔE_p (mV)
1/GO/GC	4.68	0.659	58
2/GO/GC	3.51	0.388	40
1/GO-ER/GC	9.62	0.506	23
2/GO-ER/GC	6.02	0.667	12
1/FLG/GC	0.78	0.387	85
2/FLG/GC	0.29	0.652	102

Adsorption time study

We have studied the effect of adsorption time in the amount of electroactive molecule adsorbed onto the electrode surface. GO/GC, GO-ER/GC and FLG/GC electrodes were immersed in 0.36 mM solutions of **1** or **2** in DMF during different times. We determined the amount of electroactive molecule adsorbed on the electrode surface from the cyclic voltammogram of the resulting modified electrode in 0.1M TBAP/DMF. Calculation of the charge associated with oxidation (Q_{ox}) of exTTF allows obtaining the effective surface coverage (Γ) according to equation (1).

$$\Gamma = Qox/nFA \qquad (1)$$

Where F is the Faraday constant (96485 C/mol), n is the number of electrons transferred in the redox process (n = 2) and A is the area of the electrode (0.07 cm^2).

As shown in Fig. S34, higher values by a factor of 4/5 times are observed for the GO-ER/GC electrode compared to the GO/GC and FLG/G electrodes. In all cases, a maximum value is reached after 15 hours. So, we chose this time for further studies.
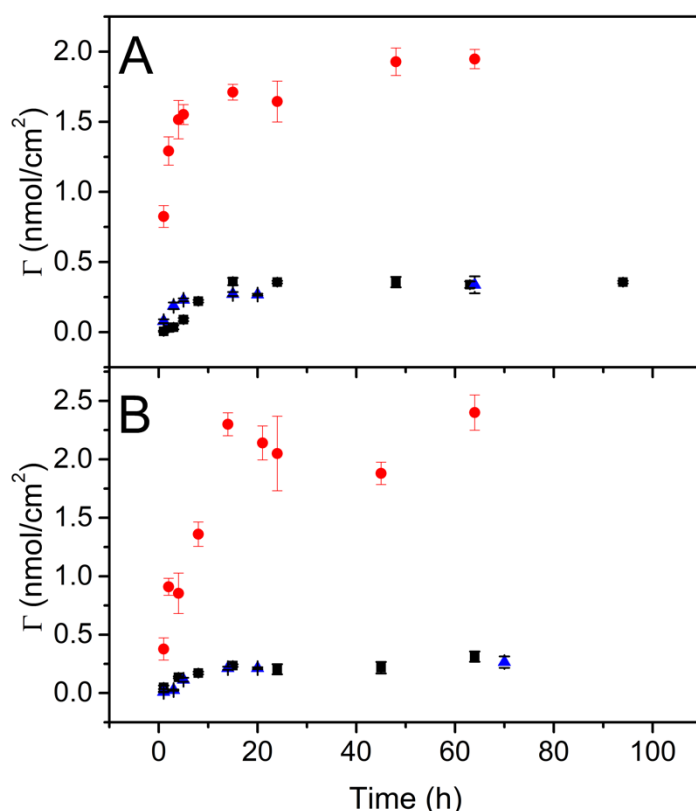

Fig. S34. Surface coverage *vs*. adsorption time of (A) **1** and (B) **2** onto GO/GC (black), GO-ER/GC (red) and FLG/GC (blue) electrodes.

Adsorptions Isotherms

We studied the adsorption process as a function of **1** or **2** concentrations, at an adsorption time of 15 hours. The data obtained were fit to Langmuir and Freundlich isotherm models. Errors bars were obtained from the standard deviation of five different electrode measurements with the same modification, in the same concentration of compounds **1** and **2** and adsorption time (15 h).

The Langmuir equation is the most widely used in adsorption studies.[22] Langmuir theory has as its basic assumption, that adsorption occurs at specific homogeneous sites inside of the adsorbent and, once an electroactive molecule occupies a site, no additional adsorption can occur there. The model is described by the equation 2.

$$\Gamma = \Gamma_s \cdot K \cdot C (K \cdot C + 1)^{-1} \qquad (2)$$

Where K is the equilibrium constant of binding and C is the concentration of adsorbate in solution and Γ_s is the saturated surface recovery.

Freundlich equation is expressed by the equation (3). The Freundlich isotherm model [23] is used for heterogeneous surface energy systems and for description of multilayer adsorption with interaction between adsorbed molecules.

$$\Gamma = K_f \cdot C^{1/n} \qquad (3)$$

Where K_f and n are the Freundlich constants. The magnitude of n gives an idea of favorability of the adsorption. A value of n between 1 and 10 indicates good adsorption capacity.

Fig. S35 shows the adsorption isotherm as surface coverage versus concentration of **1** or **2** onto the three different materials (GO/GC, GO-ER/GC and FLG/GC) and the fitting to the two different models used. shows the parameters obtained after fitting of these adsorption isotherms to the two models and the R^2, as a measure of the quality of these adjusts to the theoretical models. Obtained relative errors are only low when the model fit properly with the experimental results (Langmuir model in the case of electrochemically reduced graphene oxide), which is a clear evidence of the goodness of fits.

Table S3. Parameters obtained from the fitting to the different isotherm models.

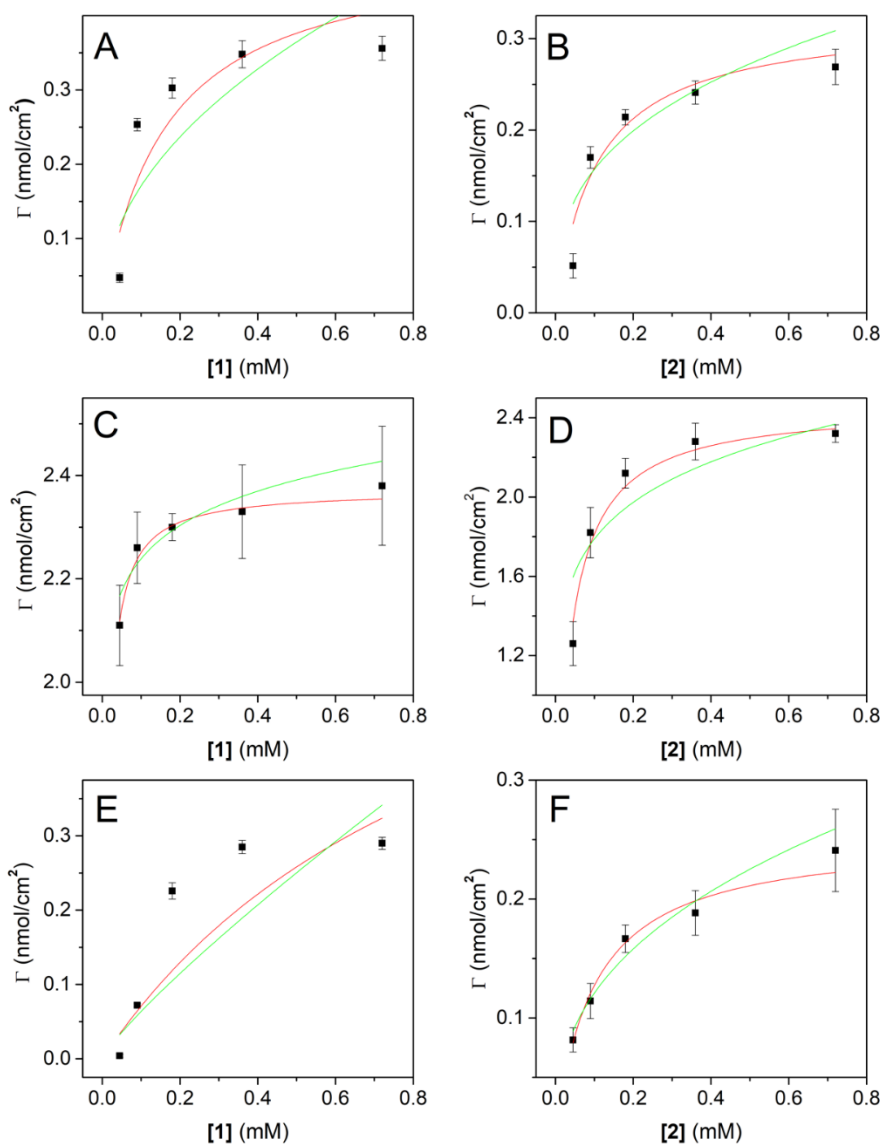|	Langmuir Isotherm					Freundlich Isotherm				
	Γ_S (mol/cm^2)	Γ_S % relative error	K	K % relative error	R^2	K_f	K_f % relative error	n	n % relative error	R^2
1/GO/GC	5.0×10^{-10}	39	6	81	0.679	5.1×10^{-10}	39	2.1	226	0.503
2/GO/GC	3.2×10^{-10}	16	10	45	0.850	3.5×10^{-10}	21	2.9	269	0.652
1/GO-ER/GC	23.7×10^{-10}	0	185	11	0.962	24.6×10^{-10}	2	24.4	383	0.778
2/GO-ER/GC	24.6×10^{-10}	2	28	15	0.962	24.8×10^{-10}	5	7.0	308	0.725
1/FLG/GC	7.7×10^{-10}	99	1	134	0.768	4.5×10^{-10}	35	1.2	359	0.719
2/FLG/GC	2.5×10^{-10}	6	10	15	0.978	2.9×10^{-10}	10	2.6	740	0.932

Fig. S35. Adsorption isotherms and data fit to Langmuir (red) and Freundlich (green) isotherm models of **1** onto GO/GC (A), GO-ER/GC (C) and FLG/GC (E) and **2** onto GO/GC (B), GO-ER/GC (D) and FLG/GC (F).
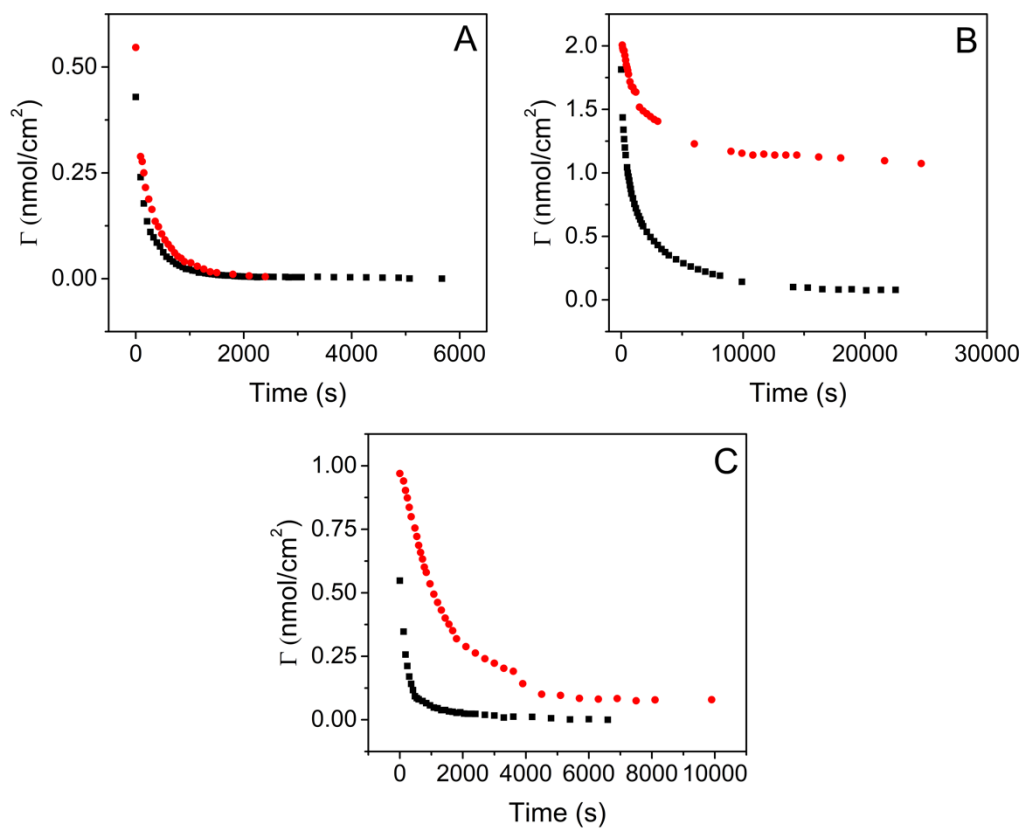
Fig. S36. Surface coverage *vs.* desorption time of modified GO/GC (A), GO-ER/GC (B) and FLG/GC (C) electrodes by adsorption of **1** (black) and **2** (red) 0.36 mM/THF for 15 hours into 0.1 M TBAP/DMF.
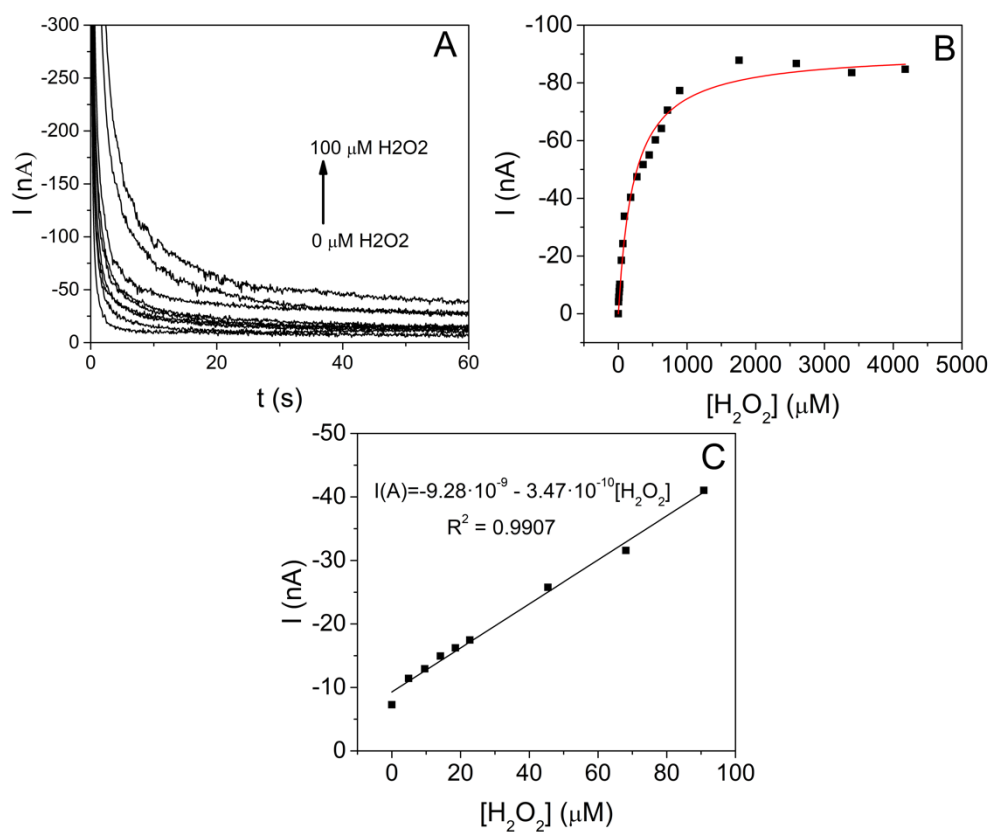
Fig. S37. (A) Chronoamperometry at 0.0 V of HRP/**1**/GO-ER/GC at 0.1 M PBS (pH = 6.5) at increasing concentrations of H_2O_2 (from 0 to 100 μM). (B) Whole range of current intensity chronoamperometry *vs.* H_2O_2 concentration. (C) Linear fit region of current intensity chronoamperometry *vs.* H_2O_2 concentration.

6. References

1. M. R. Bryce and A. J. Moore, *Synth, Met*., 1988, **25**, 203-205.
2. M. A. Herranz, C. Ehli, S. Campidelli, M. Gutiérrez, G. L. Hug, K. Ohkubo, S. Fukuzumi, M. Prato, N. Martín and D. M. Guldi, *J. Am. Chem. Soc.,* 2008, **130**, 66-73.
3. P. D. Jones and T. E. Glass, *Tetrahedron,* 2004, **60**, 11057-11065.
4. M. C. Díaz, B. M. Illescas, C. Seoane and N. Martín, *J. Org. Chem.,* 2004, **69**, 4492-4499.
5. J. A. Mann, J. Rodríguez-López, H. D. Abruña and W. R. Dichtel, *J. Am. Chem. Soc.* 2011, **133**, 17614-17617.
6. Y. Xu, H. Bai, G. Lu, C. Li and G. Shi, *J. Am. Chem. Soc*. 2008, **130**, 5856-5857.
7. a) W. S. Hummers and R. E. Offeman, *J. Am. Chem. Soc.,* 1958, **80**, 1339. b) E. Casero, A. M. Parra-Alfambra, M. D. Petit-Domínguez, F. Pariente, E. Lorenzo and C. Alonso, *Electrochemistry Communications*, 2012, **20**, 63-66. c) E. Casero, C. Alonso, L. Vázquez, M. D. Petit-Domínguez, A. M. Parra-Alfambra, M. de la Fuente, P. Merino, S. Álvarez-García, A. de Andrés, F. Pariente and E. Lorenzo, *Electroanalysis*, 2013, **25**, 154-165.
8. H.-L. Guo, X.-F. Wang, Q.-Y. Qian, F.-B. Wang and X.-H. Xia, *ACS Nano*, 2009, **3**, 2653-2659.
9. J. C. Phillips, R. Braun, W. Wang, J. Gumbart, E. Tajkhorshid, E. Villa, C. Chipot, R.D. Skeel, L. Kalé and K. Schulten, *J. Comput. Chem.,* 2005, **26**, 1781-1802.
10. S. E. Feller, Y. Zhang, R. W. Pastor and B. R. Brooks, *J. Comput. Chem*. 2005, **26**, 1781-1802.
11. T. Darden, D. York and L. Pedersen, *J. Chem. Phys.,* 1993, **98**, 10089-10092.
12. K. Vanommeslaeghe, E. Hatcher, C. Acharya, S. Kundu, S. Zhong, J. Shim, E. Darian, O. Guvench, P. Lopes, I. Vorobyov and A. D. MacKerell, *J. Comput. Chem.*, 2010, **31**, 671-690.
13. W. Yu, X. He, K. Vanommeslaeghe and A. D. MacKerell Jr., *J. Comput. Chem*., 2012, **33**, 2451-2468.
14. a) K. Vanommeslaeghe and A. D. MacKerell, *J. Chem. Inf. Model.,* 2012, **52**, 3144-3154. b) K. Vanommeslaeghe, E. P. Raman and A. D. MacKerell, *J. Chem. Inf. Model.,* 2012, **52**, 3155-3168.
15. L. Martínez, R. Andrade, E. G. Birgin and J. M. Martínez, *J. Comput. Chem.,* 2009, **30**, 2157-2164.
16. N. L. Allinger, Y. H. Yuh and J. H. Lii, *J. Am. Chem. Soc.,* 1989, **111**, 8551-8566.
17. J. W. Ponder, *TINKER Version 7.1*, 2015, http://dasher.wustl.edu/tinker
18. Chemcraft-graphical software for visualization of quantum chemistry computations. http://www.chemcraftprog.com
19. E. F. Pettersen, T. D. Goddard, C. C. Huang, G. S. Couch, D. M. Greenblatt, E. C. Meng and T. E. Ferrin, *J. Comput. Chem.,* 2004, **25**, 1605-1612.
20. M. A. Herranz, L. Yu, N. Martín and L. Echegoyen, *J. Org. Chem.,* 2003, **68**, 8379-8385.
21. A. Le Goff, B. Reuillard and S. Cosnier, Langmuir, 2013, **29**, 8736-8742.
22. I. Langmuir, *J. Am. Chem. Soc.,* 1918, **40**, 1361-1403.
23. H. Freundlich, *Zeitschrift far Chemie und Industrie der Kolloide,* 1907, **2**, 65-70.